Low Velocity Zones in the Martian Upper Mantle Highlighted by Sound Velocity Measurements

F. Xu, N. Siersch, S. Gréaux, A. Rivoldini, H. Kuwahara, N. Kondo, N. Wehr, N. Menguy, Y. Kono, Y. Higo, et al.

Low Velocity Zones in the Martian Upper Mantle Highlighted by Sound Velocity Measurements

F. Xu[1,†,‡], N. C. Siersch[1,‡], S. Gréaux[2], A. Rivoldini[3], H. Kuwahara[2,4], N. Kondo[2], N. Wehr[5], N. Menguy[1], Y. Kono[2], Y. Higo[6], A.-C. Plesa[7], J. Badro[5], D. Antonangeli[1]

[1] Sorbonne Université, Muséum National d'Histoire Naturelle, UMR CNRS 7590, Institut de Minéralogie, de Physique des Matériaux et de Cosmochimie, IMPMC, Paris, France

[2] Geodynamics Research Center, Ehime University, Matsuyama, Japan

[3] Royal Observatory of Belgium, Brussels, Belgium

[4] Institute for Planetary Materials, Okayama University, Misasa, Tottori, Japan

[5] Université de Paris, Institut de physique du globe de Paris, CNRS, Paris, France

[6] Japan Synchrotron Radiation Research Institute, SPring-8, Hyogo, Japan

[7] DLR Institute of Planetary Research, Berlin, Germany

Corresponding author: Daniele Antonangeli (daniele.antonangeli@upmc.fr)

[†] Current address: Department of Earth Sciences, University College London, London, United Kingdom

[‡] Equal contributing authors

Key Points:

- Sound wave velocities and density were measured for pressures, temperatures and mineralogical assemblages representative of Mars' mantle
- Experimental results support the existence of a low shear velocity layer in the shallow Martian mantle

- Phase equilibria experiments suggest the existence of ferrian minerals in the oxidized regions of the uppermost Martian mantle

Abstract

The InSight mission to Mars is currently monitoring the seismic activity of the planet. Interpretation of seismological observations in terms of composition and mineralogy requires the knowledge of density and thermo-elastic properties of constituent materials at pertinent conditions. We thus performed phase equilibria experiments and carried out sound velocity and density measurements on aggregates representative of the Martian mantle over pressures and temperatures directly relevant for Mars' upper and mid mantle. Our results indicate the stability of magnetite, although in a small amount, in phase assemblages at upper mantle conditions, especially in an oxidized environment. The measured pressure and temperature derivatives of compressional and shear velocities show that the temperature-induced reduction of seismic wave speeds dominates over pressure-induced effects at Mars' shallow mantle conditions for the predicted areotherms and, independently from mineralogy, support the presence of a low-shear-wave-velocity layer between 150 and 350 km depth, in agreement with seismic observations.

Plain Language Summary

The InSight mission operating on Mars is currently monitoring the planet's seismic activity. The recorded marsquakes can be used to obtain information on Mars' internal composition. However, the interpretation of these observations requires knowledge of the physical properties of the minerals expected to compose the Martian mantle at the relevant conditions. In this study we report: 1) experiments investigating the nature and abundance of the mineral phases stable at Martian mantle conditions; 2) sound velocity and density measurements on these rocks over a pressure and temperature range directly relevant for Mars' mantle, providing information that can be directly compared to the seismological findings from the InSight mission. Our results reveal the stability of small amounts of magnetite, an Fe^{3+}-rich mineral not reported in previous studies but a likely candidate in Mars' oxidized mantle environment. Moreover, measured wave velocities indicate the existence of a region between 150 and 350 km depth where, due to large temperature-induced reduction, shear wave velocities decrease with depth as opposed to an expected increase. This finding is consistent with recent observations from the InSight mission on Mars.

1 Introduction

The NASA's Discovery program mission InSight is the first mission, almost 40 years after the end of Viking 2 lander operations (Anderson et al., 1977), aiming at investigating the seismology of a rocky planetary body other than the Earth and the Moon. The spacecraft successfully landed on Mars in November 2018 (Banerdt et al., 2020) and since early winter 2019, its seismometer SEIS is continuously recording global seismic activity (Giardini et al., 2020). In the first year of operations, three quakes were strong enough to perform single station seismic analyses of Mars' subsurface and upper crust (Lognonné et al., 2020; Knapmeyer-Endrun et al., 2021). Observations of direct and reflected body-wave phases from these and few other marsquakes have been used to provide first constraints on seismic structure to a depth of 800 km (Khan et al., 2021) and the size of the core (Stähler et al., 2021). However, in order to invert seismic models for information on the composition and mineralogy of Mars' interior, knowledge of the sound velocities and density of relevant minerals and mineralogical assemblages at pertinent thermodynamic conditions are critically needed. Furthermore, most of the Martian seismic data available so far do not allow for independent source localization (Giardini et al., 2020) and a-priori knowledge of sound velocity variations as a function of pressure and temperature would play an essential role in interpreting the nature and depths of the observed seismic events. Self-consistent thermodynamic mineralogy and seismic wave velocity models of the Martian mantle have been computed for a series of pressure-temperature profiles and for a selection of bulk chemical compositions (Smrekar et al., 2019 and references therein) along self-consistent adiabats by Gibbs free-energy minimization (Connolly, 2009) using the thermodynamic formulation of Stixrude & Lithgow-Bertelloni (2005, 2011). While internally consistent, these calculations rely on available thermodynamic databases (e.g. Stixrude & Lithgow-Bertelloni, 2011; Holland et al., 2013), which have been largely constructed on the basis of minerals with compositions relevant to Earth's mantle. Experiments and calculations have not yet sufficiently constrained the thermoelastic properties of Fe-rich end members, especially Fe^{3+}-rich, minerals across the full range of pressure and temperature of Mars' mantle. Since Mars' mantle is believed to be especially enriched in Fe (Fe# = [Fe/(Fe+Mg)]x100 = 25, e.g. Dreibus & Wänke, 1985) compared to Earth's mantle (Fe# = 10, e.g. Takahashi, 1986), potentially with oxidized regions in its uppermost part (Tuff et al., 2013), current estimations do not encompass the full range of possibilities, and proposed velocity models are based on, and possibly biased by, an incomplete dataset.

The only experimental study so far investigating the phase assemblages of Mars' mantle has been performed by Bertka & Fei (1997). The synthetized aggregates at Mars' upper mantle conditions were predominantly made of olivine and pyroxene down to ~200 km depth corresponding to ~2 GPa. From this depth, pyroxene dissolves into garnet through the entire upper mantle, until olivine transforms into wadsleyite at ~1100 km depth (13.5 GPa), marking the beginning of the Martian counterpart of the transition zone as defined for the Earth's mantle (Bertka & Fei, 1997). The compositions of the olivine and pyroxene phases measured by Bertka & Fei (1997) were found to be characterized by 25 mol.% of the respective Fe end-member. Despite the reducing conditions in the experiments (both of the starting material and synthesis setup), the garnets present in the assemblages representative of the upper mantle contain not only 21 mol.% almandine ($Fe^{2+}_3Al_2Si_3O_{12}$) component, but also 5 mol.% of the skiagite ($Fe^{2+}_3Fe^{3+}_2Si_3O_{12}$) component, the latter being a Fe^{3+}-rich end-member of garnet whose thermoelastic properties have not been studied in much detail, especially lacking high-temperature data (Woodland et al., 1999; Ismailova et al., 2017; Vasiukov et al., 2018). Since Mars is believed to have oxidized regions at least in the uppermost mantle (Tuff et al., 2013), studying more oxidizing conditions during phase equilibria experiments in order to obtain mineralogical assemblages which are potentially more representative of the Martian mantle is essential.

Here we measured the bulk compressional (v_P) and shear (v_S) wave velocities as well as densities of representative Martian upper mantle mineral aggregates synthesized at various redox conditions by means of in situ ultrasonic experiments combined with synchrotron radiation at pressures and temperatures relevant to the Martian upper mantle. Our results provide direct guidance to the interpretation of seismic observations and extend on available datasets for thermodynamic models.

2 Materials and Methods

Homogeneous spherical glass samples (diameter ~ 2.5-3 mm) were produced in an aerodynamic levitation laser furnace, by fusing a powder mixture with bulk composition close to the one proposed by Taylor (2013) (oxides expected to be present at a level below 1 wt.% were not included in the starting material), employing different gas mixtures (Ar, CO_2, H_2), and quenching the melt. The glass spheres were then polished to cylinder shapes and re-equilibrated in

a multi-anvil or a piston-cylinder press, to crystallize phase assemblages analogous of the Martian mantle at high pressure and temperature (UM1 at 3 GPa and 1373 K; UM2 at 3 GPa and 1473 K; MM1 at 8 GPa and 1473 K, see Table S1). All recovered samples were well sintered. Assemblages were further analyzed using a scanning electron microscope (SEM) and electron microprobe (EMP)/ transmission electron microscope (TEM) to determine grain size, mineral phases and compositions (Table 1 and S1). For more detailed information please refer to the Supporting Information.

Sound wave velocity and density measurements were carried out at the beamline BL04B1, SPring-8, Japan, in three in situ experiments using combined ultrasonic interferometry, X-ray radiography and X-ray diffraction under high-pressure and high-temperature. Measurements have been conducted up to 6.8(1) GPa and 900 K for the upper mantle assemblages, and up to 10.6(1) GPa and 1200 K for the mid-mantle assemblage (see Supporting Information and Figure S1). The two-way travel time (t) was measured by the pulse echo method, analyzing the time delay between the buffer and sample echoes (Figure S2). At each pressure and temperature, the sample length (L) was measured by X-ray radiography, imaging two gold foils placed at both ends of the sample (Figure S3), and the compressional and shear wave velocities were calculated using the relation $= \frac{2L}{t}$. The pressure and temperature dependences of each mineralogical assemblage were derived by global fitting the respective P-T-v_P-v_S datasets to a linear function following:

$$v_{P,S} = v_{0P,S} + \partial(v_{P,S})/\partial P * P + \partial(v_{P,S})/\partial T * (T - 300K)$$

(see also Figure S4).

Energy-dispersive diffraction patterns were collected for both the samples (Figure S5) and pressure marker using a solid-state Ge-detector at a fixed 2θ angle of ~ 6°. The unit-cell volumes of the Au pressure marker were used to determine the pressure at each temperature point according to the P-V-T equation of state of gold (Tsuchiya, 2003). The unit-cell parameters of olivine, orthopyroxene, garnet and magnetite, if detected (Table S2), were determined using full profile LeBail refinements within the GSAS software package in the EXPGUI interface (Toby, 2001; Larson & Von Dreele, 2004).

3 Results and Discussion

The three aggregates show distinct mineralogies, mainly differing in proportions of olivine, pyroxene, garnet, and, when present, magnetite (Figure S6). The phase assemblages equilibrated at Martian upper mantle *P-T* conditions (UM1 and UM2) are comparable in terms of phase proportions and compositions (Table 1), with 50-54 vol.% olivine, 43-44 vol.% orthopyroxene and 3-6 vol.% magnetite, as determined from analysis of SEM and TEM images (see Supporting Information). Differently from the results of Bertka & Fei (1997), garnet is absent in these samples due to the stabilization of magnetite (Table S3). Clinopyroxene shows a small grain size, i.e. <500 nm, making it only observed in TEM composition mapping but not detectable by SEM and EPMA measurements (Table 1, Table S3). The Fe# of olivine in both assemblages is identical (Fe# = 23), whereas in orthopyroxene, the Fe# of UM1 is 20 compared to a Fe# = 22 in UM2, which can be attributed to the fact that 3 vol.% more Al-Mg-rich magnetite is present in UM1 than in UM2 incorporating some amount of Fe into its structure. Magnetite is observed in these upper mantle assemblages irrespective of the gas flux used in the glass synthesis and the capsule material used for the high *P-T* equilibrations (Table S1), and this is another major difference with respect to the previous study by Bertka & Fei (1997) (Table S3). One possible explanation is the use of Re and Pt foils and the Fe^{3+}-rich oxide mixtures as starting material in this study, in contrast to the more reducing conditions imposed by the capsule materials (graphite-lined Pt capsules) containing the previously reduced starting material used by Bertka & Fei (1997). Noteworthy, a recent study reported the stability of magnetite next to majoritic garnet and pyroxene when starting from a bulk composition similar to the one investigated here (Tao et al., 2018). More importantly, the presence of Fe^{3+} bearing phases, and possibly magnetite, in the Martian mantle assemblage is reasonable under the assumption of an Fe-rich and oxidized uppermost mantle (Tuff et al., 2013). Still, ferrian minerals have not been taken into account in any of the mineralogy and velocity models considered so far (e.g., Smrekar et al., 2019 and references therein).

The phase assemblage of the run under mid-mantle *P-T* condition (MM1) contains 23 vol.% of garnet, 30 vol.% of orthopyroxene and 47 vol.% of olivine (Table 1). The Fe# in olivine and orthopyroxene are 23 and 18, respectively, with the garnet being rich in Fe^{3+}, containing 23 mol.% skiagite ($Fe^{2+}_3Fe^{3+}_2Si_3O_{12}$) and 18 mol.% andradite ($Ca_3Fe^{3+}_2Si_3O_{12}$) components. Such an

enrichment in Fe^{3+} is significant, especially if compared to the previous phase equilibrium study (Bertka & Fei, 1997).

The compressional and shear wave velocities for all three runs increase monotonically with pressure and decrease with increasing temperatures (e.g. UM2 in Figures S4). Both v_P and v_S for the upper mantle experiments UM1 and UM2 are very similar, within mutual uncertainties (Table S4). This observation can be readily explained in view of the similar phase assemblages and mineralogy of the two samples. The wave velocities v_P and v_S for the mid-mantle experiment MM1 are higher than those measured for the upper mantle experiments (Table S4) and with a larger increase with increasing pressure, presumably related to the presence of garnet in this phase assemblage (Table S1).

Using the derivatives of v_P and v_S with respect to T and P from the experimental dataset of this study (Table S5), v_P and v_S of each phase assemblage are calculated as a function of depth along two different Martian mantle temperature profiles (areotherms) (Figure 1). These areotherms are chosen as representative cases out of a larger series established by recent 3-D thermal evolution models (Plesa et al., 2018). Both areotherms have been calculated assuming a crustal heat production rate compatible with the surface abundance of heat producing elements measured by the gamma ray spectrometer instrument onboard Mars Odyssey (Taylor et al., 2006; Hahn et al., 2011). Case 12 is representative for a relatively thin crust (45 km) that contains about 44% of the total bulk amount of heat producing elements and is characterized by a steep temperature increase down to depths of ~350 km, from where the temperature profile flattens out towards the lower mantle (Figure S7). Case 56 considers a thick crust (87.1 km) that contains most of the heat producing elements, i.e., 94%, leading to an overall less pronounced temperature increase at shallow depths. In this latter case, the areotherm starts flattening out at a depth of 800 km reaching a temperature approximately 420 K lower compared to case 12 (Figure S7). From our experimental data we predict a low-velocity layer, i.e., a decrease in wave velocities with increasing depth, at shallow mantle depths (~150-350 km depths range) for both v_P and v_S for the thin-crust areotherm (case 12). For the thick-crust areotherm (case 56), a low-velocity layer is present for v_S, whereas variation of v_P with depth (initial small reduction followed by a slight increase) are too small to derive firm conclusions. Results along more areotherms for thin and thick crust and different thermal evolution models (Plesa et al., 2018) are shown in the Supporting Information (Figure S8). Different temperature profiles affect absolute values of velocities, but not the overall behavior with

depth for the two classes of areotherms (i.e. thin and thick crust). The occurrence of extended low-shear-velocity zones is predicted for all phase assemblages considered here and can be explained by the temperature-induced velocity decrease prevailing over the pressure-induced velocity increase at depths shallower than 400 km.

The obtained experimental results along the case 12 areotherm are compared to wave velocities modelled along the same areotherm for aggregates having the same bulk composition of the experiments but assuming all Fe to be present as Fe^{2+} due to the absence of Fe^{3+} in end-member phases in the Stixrude & Lithgow-Bertelloni (2011) database (Figure 2). Specifically, equilibrium phase assemblages are determined by Gibbs free energy minimization using Perple_X (Connolly, 2009) (Table S3), and the elastic properties of the aggregates are computed with the thermodynamic formulation and thermodynamic database of Stixrude & Lithgow-Bertelloni (2005, 2011). The overall agreement between experiment-based velocity profiles and models is good, in particular for the mid-mantle assembly, where the two are within uncertainties. For upper-mantle assemblies modeled v_P is below (UM1) or above (UM2) experiment-based velocity profiles by ~1%, while v_S is below by ~2% in the case of UM1 or close for UM2. Accordingly, neglecting the presence of Fe^{3+} bearing minerals leads to less than 2% difference between the results obtained in our experiments and self-consistent thermodynamic models.

The experimental results along the areotherm case 12 are also compared to mantle velocity models (Smrekar et al., 2019) computed along the same areotherm using the thermodynamic approach detailed above (Figure 3a). Several bulk chemistry compositions proposed for the mantle of Mars are considered here - MA: Morgan & Anders, 1979; LF: Lodders & Fegley, 1997; EH45 and EH70: Sanloup et al., 1999; MM: Mohapatra & Murty, 2003; TA: Taylor, 2013; and YO: Yoshizaki & McDonough, 2020; together with the bulk chemistry of our starting material (Table 1). It is important to note that the experiment-based results are computed for constant mineralogy, corresponding to equilibrium mineralogy at depth ~250 km (UM1 and UM2) and ~650-680 km (MM1). Thermodynamic models use Gibbs free-energy minimization and thus have a mineralogy that evolves with depth. Both v_P and v_S obtained from the ultrasonic experiments and modeled for our starting composition plot on the lower end of the velocities calculated with thermodynamic models, close to estimations for the composition EH70 suggested by Sanloup et al. (1999), despite the significant difference in major element concentration (+7.3 wt.% SiO_2; -0.53 wt.% Al_2O_3, -6.7 wt.% FeO, -3.2 wt.% MgO and -0.43 wt.% CaO of EH70 with respect to our composition).

Assuming the areotherm case 56, both the experimental and calculated wave velocities increase slightly, without changes to the relative difference. Overall, we observe generally faster wave velocities from the previously published models compared to our experiments and model. The TA model, which has a bulk chemistry very close to that of our experiments, shows a v_P/v_S ratio very close to that modeled for our starting composition (Figure 3b) but absolute velocities systematically above our measurements (difference up to ~0.23 km/s and up to ~0.1 km/s for v_P and v_S, respectively). This offset can be explained by the larger amounts of clinopyroxene in the TA model (up to 19.1 %) and less orthopyroxene (13.3 %) compared to the phase proportion modeled for the starting material composition of this study, resulting in the stability of only 5.6 % of clinopyroxene and a larger amount of orthopyroxene (up to 28.2 %) (Table S3). Indeed, at pressure and temperature conditions of the case 12 areotherm clinopyroxene is faster compared to orthopyroxene (Flesch et al., 1998; Kung et al., 2005; Li and Neuville, 2010; Kung et al., 2011). In comparison to a typical mineralogy of the Earth's mantle (Ringwood, 1969), calculated along the same areotherms (Figure 3a), the wave velocities through Mars' upper and mid-mantle are significantly slower than those of the Earth, ~0.5 km/s for v_P and ~0.3 km/s for v_S. This can be attributed not only to the higher garnet and olivine over pyroxene content in the Earth, but also to the lower Fe# of ~10 assumed for the Earth versus a Fe# of ~25 expected for Mars, which has a significant effect on the bulk wave velocities (Stixrude & Lithgow-Bertelloni, 2011).

Irrespective of absolute velocity values, a low-S-wave-velocity layer at shallow depths is expected according both experiments and for all self-consistent thermodynamic models, further supporting the independence of this finding from mineralogy. Available Martian seismic records suggest a possible S-wave shadow zone at an epicentral distance range of ~40–60° from the InSight landing site (Giardini et al., 2020; Khan et al., 2021), which might result from the presence of a low-velocity layer in the upper mantle. Our experimental results and the above-presented considerations provide a direct explanation for this observation and support the existence of a low-S-wave-velocity zone in the upper mantle of Mars (Khan et al., 2021) as a direct consequence of the dominant temperature-induced effects on seismic velocities along all areotherms considered in this study (Plesa et al., 2018). Whether or not a low-P-wave-velocity layer will be observed on Mars would provide constraints on the thermal structure of the upper mantle, with a low-P-wave-velocity zone being a strong indication of hot temperatures in the shallow mantle, such as the temperature profile case 12 of Plesa et al. (2018).

The v_P/v_S ratio between 100 and 800 km depth, which directly affects the difference in the arrivals between P-waves and S-waves, is shown in Figure 3b. This ratio shows a smooth monotonic increase for all three Martian compositions investigated in this study. Within experimental uncertainties, shown as shaded areas, v_P/v_S is the same for the two upper mantle assemblages. Furthermore, the experimental data clearly falls into the same range as calculated for different Martian compositions using thermodynamic end-member data by Stixrude & Lithgow-Bertelloni (2011). Compared to a typical v_P/v_S for Earth's mantle composition (Ringwood, 1969) along a Martian temperature profile, the bulk v_P/v_S for Mars is larger, especially for depths > 400 km. Another interesting observation is that the dependence of v_P/v_S on pressure in our assemblages does not significantly vary along isotherms, for temperatures in the range of 300 - 2500 K tested by extrapolation of results in this study. Thus, the measured v_P/v_S ratio provides important constraints for the estimation of the epicentral distance of marsquakes recorded by InSight.

5 Conclusions

In this study, we report the stability of magnetite, although to a small fraction, in Martian mantle phase assemblages at conditions directly pertinent to its upper mantle, especially in an oxidized environment. Additionally, the presence of Fe^{3+}-bearing garnets was inferred in the mid-mantle phase assemblage. We thus argue for a Martian mantle mineralogy more complex compared to what has been considered so far (e.g. Bertka & Fei, 1997; Smrekar et al., 2019 and references therein). Sound velocity measurements have been carried out at high pressure and high temperature and suggest seismic wave velocities possibly slower compared to the majority of the velocity models that have been previously proposed for Mars. Whether the difference between experiments and thermodynamic models is the result of the presence of iron as Fe^{3+} or of the different phase proportions in our assemblages compare to those predicted by existing thermodynamic equilibrium calculations remains to be assessed. Nevertheless, the presence of low-S-wave-velocity layer extending between 150 and 350 km depth, and possibly up to ~500 km depth, is independent of the considered mineralogy and thermal structure and is therefore a robust conclusion that is compatible with the findings from recent InSight seismic observations (Giardini et al., 2020; Khan et al., 2021). The v_P/v_S ratio depends only weakly on mantle composition and mineralogy and is largely independent of temperature. Hence the v_P/v_S ratio that has been measured

in this study provides direct constraints for the estimation of the epicentral distance of quakes and guidance for the interpretation of seismic data collected on Mars.

Acknowledgments

We thank two anonymous reviewers for their thoughtful and constructive comments that have improved an earlier version of this paper. We also thank the editor A. J. Dombard for handling the revision process of the manuscript. The authors wish to thank Imène Estève and Stéphanie Delbrel for their help with ion-milling and sample analysis by SEM at the Institut de Minéralogie de Physique des Matériaux et de Cosmochimie (IMPMC, Paris) and Michel Fialin and Nicolas Rividi for their help during microprobe analysis at the Centre Camparis, Sorbonne Université (Paris, France). We would like to thank Stephan Borensztajn for his help with the FIB cutting at IPGP (Paris, France). This project has received funding from the European Research Council (ERC) under the European Union's Horizon 2020 research and innovation Programme (Grant agreement 724690). This work was supported by the French Space Agency (CNES), focused on SEIS instrument of the InSight mission. AR is financially supported by the Belgian PRODEX program managed by the European Space Agency in collaboration with the Belgian Federal Science Policy Office. ACP gratefully acknowledges the financial support and endorsement from the DLR Management Board Young Research Group Leader Program and the Executive Board Member for Space Research and Technology. The Focused Ion Beam (FIB) and Scanning Electron Microscope (SEM) facility at IMPMC is supported by Région Ile de France grant SESAME 2006 N°I-07-593/R, INSU-CNRS, Institute de Physique (INP)–CNRS, University Pierre et Marie Curie–Paris 6, and by the French National Research Agency (ANR) grant ANR-07-BLAN-0124-01. Infrastructures and services at the Geodynamics Research Center (GRC), Ehime University, were made available through the PRIUS program. The synchrotron radiation experiments were performed under SPring-8 Non-Proprietary Research Proposals Numbers 2019A1473 and 2019B1305, in collaboration with the partner user program (2019A0069 and 2019B0069). This paper is InSight Contribution 199. Datasets for this research (main paper and Supporting Information) are available at https://doi.org/10.5281/zenodo.4709036 (doi: 10.5281/zenodo.4709036).

References

Anderson, D.L., Miller, W.F., Latham, G. V., Nakamura, Y., Toksöz, M.N., Dainty, A.M., Duennebier, F.K., Lazarewicz, A.R., Kovach, R.L., Knight, T.C.D. (1977). Seismology on Mars. *J. Geophys. Res*. 82, 4524-4546. https://doi.org/10.1029/JS082i028p04524

Banerdt, W. B., Smrekar, S. E., Banfield, D., Giardini, D., Golombek, M., Johnson, C. L., et al. (2020). Initial results from the InSight mission on Mars. *Nature Geoscience*, *13*(3), 183–189. https://doi.org/10.1038/s41561-020-0544-y

Bertka, C. M., & Fei, Y. (1997). Mineralogy of the Martian interior up to core-mantle boundary pressures. *Journal of Geophysical Research: Solid Earth*, *102*(B3), 5251–5264. https://doi.org/10.1029/96jb03270

Connolly, J. A. D. (2009). The geodynamic equation of state: What and how. *Geochemistry, Geophysics, Geosystems*, *10*(10). https://doi.org/10.1029/2009GC002540

Dreibus, G., & Wänke, H. (1985). Mars, a volatile-rich planet. *Meteoritics*, *20*(2), 367–381.

Flesch, L. M., Baosheng Li, & Liebermann, R. C. (1998). Sound velocities of polycrystalline MgSiO3-orthopyroxene to 10 GPa at room temperature. *American Mineralogist*, *83*(5–6), 444–450. https://doi.org/10.2138/am-1998-5-604

Giardini, D., Lognonné, P., Banerdt, W. B., Pike, W. T., Christensen, U., Ceylan, S., et al. (2020). The seismicity of Mars. *Nature Geoscience*, *13*(3), 205–212. https://doi.org/10.1038/s41561-020-0539-8

Hahn, B. C., McLennan, S. M., & Klein, E. C. (2011). Martian surface heat production and crustal heat flow from Mars Odyssey gamma-ray spectrometry. *Geophysical Research Letters*, 38, L14203. https://doi.org/10.1029/2011GL047435

Holland, T. B., Hudson, N. F. C., Powell, R., & Harte, B. (2013). Newthermodynamic models and calculated phase equilibria in NCFMAS for basic and ultrabasic compositions through thetransition zone into the uppermost lower mantle. *Journal of Petrology*, *54*(9), 1901–1920. https://doi.org/10.1093/petrology/egt035

Ismailova, L., Bykov, M., Bykova, E., Bobrov, A., Kupenko, I., Cerantola, V., et al. (2017). Effect of composition on compressibility of skiagite-Fe-majorite garnet. *American Mineralogist*, *102*(1), 184–191. https://doi.org/10.2138/am-2017-5856

Larson, A. C., & Von Dreele, R. B. (2004). General structure analysis system (GSAS). *Los Alamos National Laboratory Report*, *Report*(LAUR), 86–748.

Levy, D., Diella, V., Dapiaggi, M., Sani, A., Gemmi, M., & Pavese, A. (2004). Equation of state, structural behaviour and phase diagram of synthetic MgFe2O4, as a function of pressure and temperature. *Physics and Chemistry of Minerals*, *31*(2), 122–129. https://doi.org/10.1007/s00269-004-0380-4

Khan, A., Ceylan, S., van Driel, M., Giardini, D., Lognonné, P., Samuel, H., et al. (2021). Upper mantle structure of Mars from InSight seismic data. *Science*, 373, 434-438. https://doi.org/10.1126/science.abf2966

Knapmeyer-Endrun, B., Panning, M., Bissig, Joshi, R., Khan, A., Kim, D., et al. (2021). Thickness and structure of the Martian crust from InSight seismic data. *Science*, *373*, 438-443. https://doi.org/10.1126/science.abf8966

Kung, J., Li, B., Uchida, T., & Wang, Y. (2005). In-situ elasticity measurement for the unquenchable high-pressure clinopyroxene phase: Implication for the upper mantle. *Geophysical Research Letters*, *32*(1), 1–4. https://doi.org/10.1029/2004GL021661

Kung, J., Jackson, I., & Liebermann, R. C. (2011). High-temperature elasticity of polycrystalline orthoenstatite (MgSiO 3). *American Mineralogist*, *96*(4), 577–585. https://doi.org/10.2138/am.2011.3632

Li, B., & Neuville, D. R. (2010). Elasticity of diopside to 8GPa and 1073K and implications for the upper mantle. *Physics of the Earth and Planetary Interiors*, *183*(3–4), 398–403. https://doi.org/10.1016/j.pepi.2010.08.009

Lodders, K., & Fegley, B. (1997). An oxygen isotope model for the composition of Mars. *Icarus*, *126*(2), 373–394. https://doi.org/10.1006/icar.1996.5653

Lognonné, P., Banerdt, W. B., Pike, W. T., Giardini, D., Christensen, U., Garcia, R. F., et al. (2020). Constraints on the shallow elastic and anelastic structure of Mars from InSight seismic data. *Nature Geoscience*, *13*(3), 213–220. https://doi.org/10.1038/s41561-020-0536-y

Mohapatra, R. K., & Murty, S. V. S. (2003). Precursors of Mars: Constraints from nitrogen and oxygen isotopic compositions of martian meteorites. *Meteoritics and Planetary Science*, *38*(2), 225–241. https://doi.org/10.1111/j.1945-5100.2003.tb00261.x

Morgan, J. W., & Anders, E. (1979). Chemical composition of Mars. *Geochimica et Cosmochimica Acta*, *43*(10), 1601–1610. https://doi.org/10.1016/0016-7037(79)90180-7

Plesa, A. C., Padovan, S., Tosi, N., Breuer, D., Grott, M., Wieczorek, M. A., et al. (2018). The Thermal State and Interior Structure of Mars. *Geophysical Research Letters*, *45*(22), 12,198-12,209. https://doi.org/10.1029/2018GL080728

Quinn, R.J., Valley, J.W., Page, F.Z., Fournelle, J.H. (2016). Accurate determination of ferric iron in garnets. *American Mineralogist*, 101 1704–1707. http://dx.doi.org/10.2138/am-2016-5695

Ringwood, A. E. (1969). Composition of the crust and upper mantle. *The Earth's Crust and Upper Mantle, Geophys. Monogr. Ser.* 13, 1–17.

Sanloup, C., Jambon, A., & Gillet, P. (1999). A simple chondritic model of Mars. *Physics of the Earth and Planetary Interiors*, *112*(1–2), 43–54. https://doi.org/10.1016/S0031-9201(98)00175-7

Smrekar, S. E., Lognonné, P., Spohn, T., Banerdt, W. B., Breuer, D., Christensen, U., et al. (2019). Pre-mission InSights on the Interior of Mars. *Space Science Reviews* 215,. 1–72. https://doi.org/10.1007/s11214-018-0563-9

Stähler, S. C., Khan, A., Banerdt, W. B., Lognonné, P., Giardini, D., Ceylan, S., et al. (2021). Seismic detection of the Martian core. *Science*, *373*, 443-448. https://doi.org/10.1126/science.abi7730

Stixrude, L., & Lithgow-Bertelloni, C. (2005). Thermodynamics of mantle minerals - I. Physical properties. *Geophysical Journal International*, *162*(2), 610–632. https://doi.org/10.1111/j.1365-246X.2005.02642.x

Stixrude, L., & Lithgow-Bertelloni, C. (2011). Thermodynamics of mantle minerals - II. Phase equilibria. *Geophysical Journal International*, *184*(3), 1180–1213. https://doi.org/10.1111/j.1365-246X.2010.04890.x

Takahashi, E. (1986). Melting of a dry peridotite KLB-1 up to 14 GPa: Implications on the Origin of peridotitic upper mantle. *Journal of Geophysical Research*, *91*(B9), 9367. https://doi.org/10.1029/jb091ib09p09367

Tao, R., Fei, Y., Bullock, E. S., Xu, C., & Zhang, L. (2018). Experimental investigation of Fe3+-rich majoritic garnet and its effect on majorite geobarometer. *Geochimica et Cosmochimica Acta*, *225*, 1–16. https://doi.org/10.1016/j.gca.2018.01.008

Taylor, G. J., Boynton, W., Brückner, J., Wänke, H., Dreibus, G., Kerry, K., et al. (2006). Bulk composition and early differentiation of Mars. Journal of Geophysical Research, 111, E03S10. https://doi.org/10.1029/2005JE002645.

Taylor, G. J. (2013). The bulk composition of Mars. *Chemie Der Erde*, *73*(4), 401–420. https://doi.org/10.1016/j.chemer.2013.09.006

Toby, B. H. (2001). EXPGUI, a graphical user interface for GSAS. *Journal of Applied Crystallography*, *34*(2), 210–213. https://doi.org/10.1107/S0021889801002242

Tsuchiya, T. (2003). First-principles prediction of the P - V - T equation of state of gold and the 660-km discontinuity in Earth's mantle . *Journal of Geophysical Research: Solid Earth*, *108*(B10), 311–328. https://doi.org/10.1029/2003jb002446

Tuff, J., Wade, J., & Wood, B. J. (2013). Volcanism on Mars controlled by early oxidation of the upper mantle. *Nature*, *498*(7454), 342–345. https://doi.org/10.1038/nature12225

Vasiukov, D. M., Ismailova, L., Kupenko, I., Cerantola, V., Sinmyo, R., Glazyrin, K., et al. (2018). Sound velocities of skiagite–iron–majorite solid solution to 56 GPa probed by

nuclear inelastic scattering. *Physics and Chemistry of Minerals*, *45*(5), 397–404. https://doi.org/10.1007/s00269-017-0928-8

Woodland, A. B., Angel, R. J., Koch, M., Kunz, M., & Miletich, R. (1999). Equations of state for Fe 3 2+ Fe 2 3+ Si 3 O 12 “skiagite” garnet and Fe 2 SiO 4 -Fe 3 O 4 spinel solid solutions . *Journal of Geophysical Research: Solid Earth*, *104*(B9), 20049–20058. https://doi.org/10.1029/1999jb900206

Yoshizaki, T., & McDonough, W. F. (2020). The composition of Mars. *Geochimica et Cosmochimica Acta*, *273*, 137–162. https://doi.org/10.1016/j.gca.2020.01.011

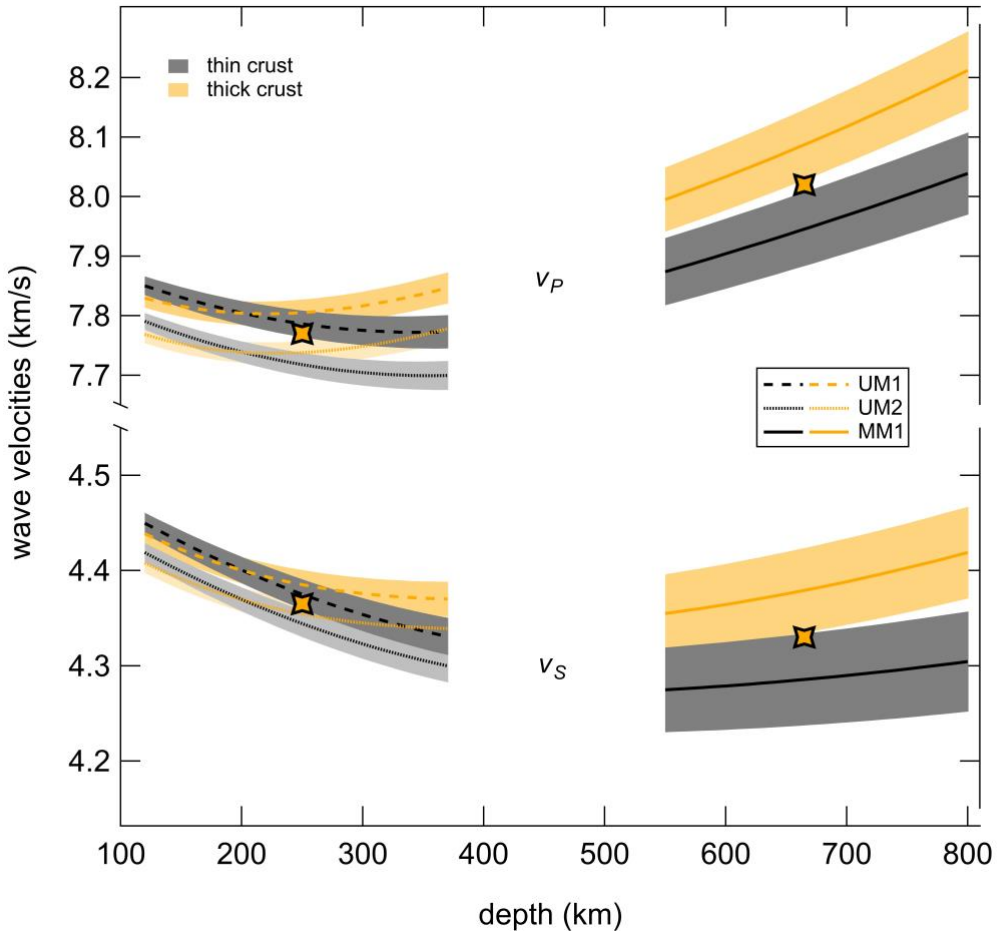

Figure 1. Experiment-based compressional v_P and shear wave velocities v_S of three different mineralogical assemblages versus depth along two different areotherms. The black and orange lines represent the two areotherms assuming a thin crust (case12, 45 km) or thick crust (case 56, 87.1 km), respectively. Extended low-velocity zones are visible for v_S in both cases. V_P shows a low-velocity zone only for the thin crust areotherm (case 12). The shaded areas represent the experimental uncertainties. Results are for constant mineralogy, corresponding to equilibrium mineralogy at depth ~250 km (UM1 and UM2) and ~650-680 km (MM1), indicated as stars in the figure.

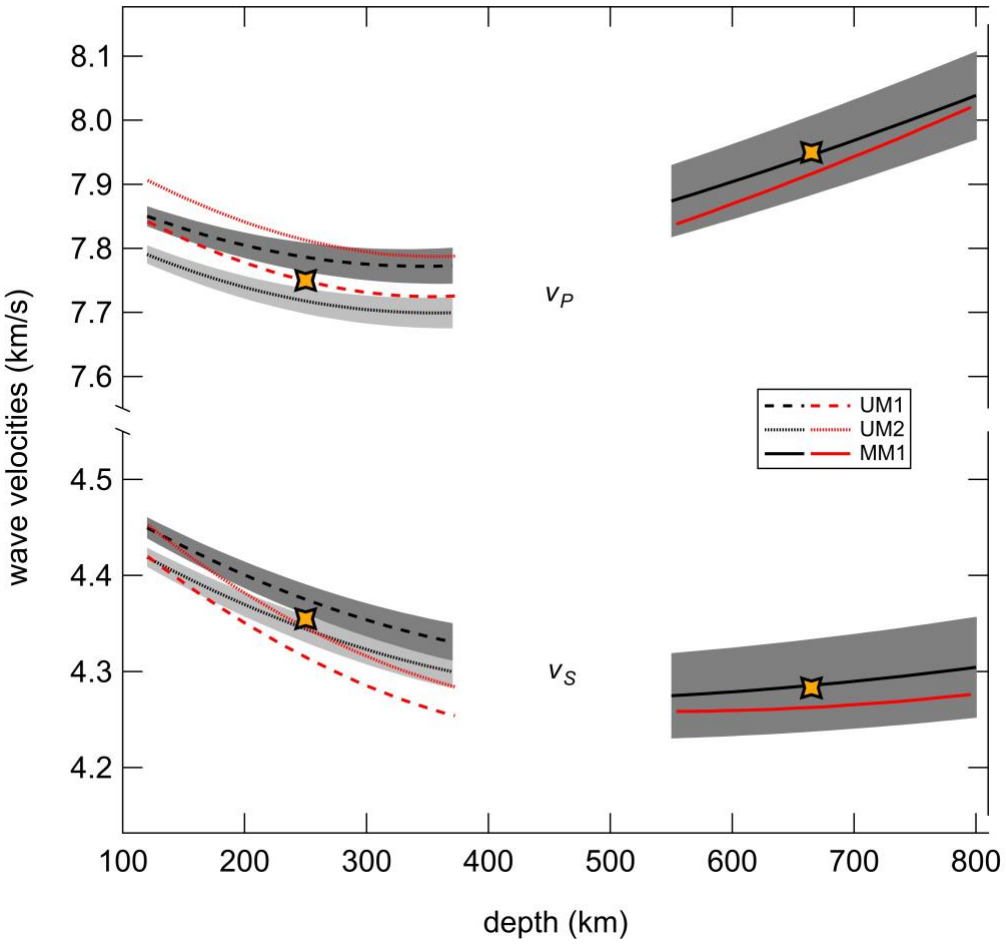

Figure 2. Experiment-based compressional v_P and shear wave velocities v_S of three different mineralogical assemblages versus depth along a thin crust areotherm (case 12, 45 km average crustal thickness, black) in comparison to velocities according to

thermodynamic calculations (red lines). The modelled velocities were calculated using the thermodynamic formulation of Stixrude & Lithgow-Bertelloni (2005) and parameters of Stixrude & Lithgow-Bertelloni (2011) for composition Bulk (2) (see Table 1), but assuming all Fe to be present as Fe^{2+} due to the absence of Fe^{3+} in end-member phases in the Stixrude & Lithgow-Bertelloni (2011) database. Calculations for composition Bulk (1) differ at most by 0.05 km/s for v_P and 0.03 km/s for v_S. The shaded areas represent the experimental uncertainties. Noteworthy, while experimental results are for constant mineralogy, corresponding to equilibrium mineralogy at depth ~250 km (UM1 and UM2) and ~650-680 km (MM1), indicated as stars in the figure, thermodynamic models have mineralogy resulting from Gibbs free-energy minimization and thus evolving with depth.

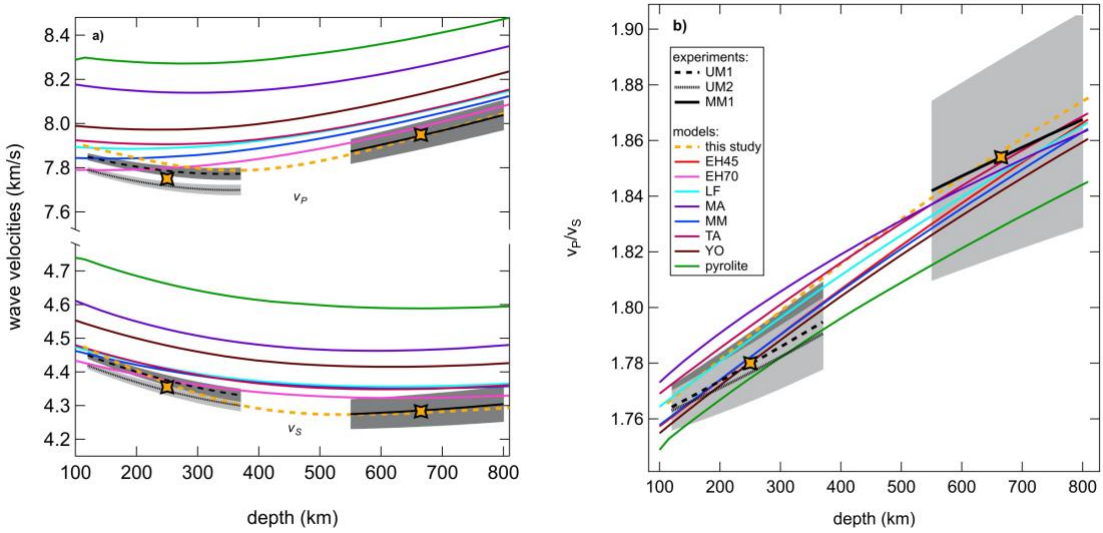

Figure 3. Experiment-based compressional v_P and shear wave velocities v_S (a) and v_P/v_S (b) of three different mineralogical assemblages studied here versus depth along the thin crust areotherm case 12 (45 km average crustal thickness). The grey shaded areas represent the experimental uncertainties. Self-consistent thermodynamic models (colored lines) calculated for different bulk starting compositions proposed in literature show wave velocities faster than the experimental ones. We note, however, that experimental results are for constant mineralogy, corresponding to equilibrium mineralogy at depth ~250 km (UM1 and UM2) and ~650-680 km (MM1), indicated as stars in the figure, while self-consistent thermodynamic models have been computed for mineralogy evolving with depth.

Tables

Table 1. Phase proportions of measured samples and compositions of constituent phases. The bulk composition of each sample is estimated in two different ways: (1) by SEM analysis performed over large window scans (200 x 200 μm) and averaged over multiple areas of the sample; and (2) from the phase proportions determined from the SEM/TEM images and compositions of each phase. In case (1) all Fe is counted as FeO. The starting chemical composition of oxide mixture is in wt.% SiO_2: 44.6; Al_2O_3: 3.1; FeO: 18.5; MgO: 31.2; CaO: 2.5. Phases are olivine (Ol), orthopyroxene (Opx), garnet (Gt) and magnetite (Mag).

Run NO.	Ol	Opx[a]	Gt	Mag	Bulk (1)	Bulk (2)
UM1 (TEM) 3 GPa, 1373K, 1 hour[b]						
SiO_2	39.0	53.2		1.4	45.7	43.2
Al_2O_3	-	3.7		10.0	3.2	2.2
FeO[c]	21.1	11.8		24.1	19.3	17.1
Fe_2O_3[c]	-	1.9		59.1	-	4.1
MgO	39.8	27.4		5.3	29.7	32.4
CaO	0.1	2.0		0.1	2.0	1.0
UM2 (EMP) 3 GPa, 1473K, 24 hours						
SiO_2	39.4	50.9		1.6	46.4	42.4
Al_2O_3	0.5	4.3		14.3	3.3	3.0
FeO	20.6	7.7		21.2	18.1	14.9
Fe_2O_3	-	6.9		55.2	-	6.1
MgO	39.0	28.3		7.5	29.5	32.5
CaO	0.5	1.9		0.1	2.8	1.1
MM1[d] (EMP) 8 GPa, 1473K, 23 hours						
SiO_2	39.1	55.7	40.3		45.8	44.3
Al_2O_3	0.2	0.5	10.9		3.3	2.9
FeO	21.1	11.3	8.8		18.6	15.3
Fe_2O_3	-	1.3	17.1		-	4.4
MgO	39.2	30.0	15.9		29.8	31.0
CaO	0.4	1.2	6.9		2.5	2.2
Phase proportion						
UM1	44	50		6		
UM2	43	54		3		
MM1	47	30	23			

[a] Only orthopyroxene was counted here due to the non-detection of clinopyroxene in SEM and EMP measurement. (see also table S3).

[b] The TEM or EMP in the parathesis indicate the composition was obtained by TEM or EMP analysis, respectively. Pressure, temperature and duration of the synthesis run are also indicated.

[c] The valence states iron in Opx, Gt and Mag was calculated according to the charge balance method (Quinn et al., 2016). See supplement S2 for more details.

[d] Composition was measured after synthesis, before sound wave velocity measurement.

Supporting Information for

Low Velocity Zones in the Martian Upper Mantle Highlighted by Sound Velocity Measurements

F. Xu[1,†,‡], N. C. Siersch[1,‡], S. Gréaux[2], A. Rivoldini[3], H. Kuwahara[2,4], N. Kondo[2], N. Wehr[5], N. Menguy[1], Y. Kono[2], Y. Higo[6], A.-C. Plesa[7], J. Badro[5], D. Antonangeli[1]

[1] Sorbonne Université, Muséum National d'Histoire Naturelle, UMR CNRS 7590, Institut de Minéralogie, de Physique des Matériaux et de Cosmochimie, IMPMC, Paris, France

[2] Geodynamics Research Center, Ehime University, Matsuyama, Japan

[3] Royal Observatory of Belgium, Brussels, Belgium

[4] Institute for Planetary Materials, Okayama University, Misasa, Tottori, Japan

[5] Université de Paris, Institut de physique du globe de Paris, CNRS, Paris, France

[6] Japan Synchrotron Radiation Research Institute, SPring-8, Hyogo, Japan

[7] DLR Institute of Planetary Research, Berlin, Germany

Corresponding author: Daniele Antonangeli (daniele.antonangeli@upmc.fr)

† Current address: Department of Earth Sciences, University College London, London, United Kingdom

‡ Equal contributing authors

Introduction

In section S1 to S4 we provide more detailed information on sample synthesis, sample characterization, in situ synchrotron experiments and data analysis. In section S5 we provide additional discussion about sample's density, bulk and shear moduli. Figure S1 shows the *P-T* path followed in the three in-situ ultrasonic interferometry and X-ray diffraction experiments. Figure S2 and S3 show a representative ultrasonic signal and a typical X-ray radiography image, respectively, of sample MM1 at 7.9 GPa and 1000 K. Figure S4 shows the wave velocities and densities versus pressure of sample UM2 collected along isotherms. Figure S5 shows typical energy-dispersive X-ray diffraction pattern collected for the upper mantle experiment UM1. Figure S6 shows representative backscattered electron images for the three mineralogical assemblages here investigated. Figure S7 shows two representative areotherms used in this study selected from the larger set in Plesa et al. (2018). Figure S8 provides wave velocities as a function of depth along six areotherms representative for Mars. Figure S9 shows the bulk density of studied mineralogical assemblages versus pressure at 300 K. Figure S10 shows the bulk density of the three phase assemblages investigated in this study along the case 12 areotherm. Figure S11 shows the adiabatic bulk modulus K_S and shear modulus G for the three bulk assemblages studied versus depth. Table S1 provides the experimental conditions and run products of all synthesis experiments. Table S2 reports unit-cell lattice parameters and densities of all phases present in the three mineralogical assemblages as determined from energy-dispersive X-ray diffraction. Table S3 outlines the phase proportion obtained in this study by experimental observations and modeling in comparison with the previous report by Bertka & Fei (1997). Table S4 shows the experimental pressure and temperature,

compressional (v_P) and shear (v_S) wave velocities, and densities of measured samples and Table S5 reports the results of 2-Dimensional global linear fitting for velocity and density according to the equation $M = M_0 + \partial M/\partial P * P + \partial M/\partial T * (T - 300\,K)$ with M= $\{v_P, v_S, \rho\}$.

S1. Samples' synthesis

Starting material with composition in weight percent of oxides close to the one proposed by Taylor (2013) (oxides expected to be present at a level below 1 wt.% were not included in the starting material) was prepared from synthetic SiO_2, Al_2O_3, Fe_2O_3, MgO and $CaCO_3$ powders that were ground in an agate mortar under ethanol for 1 h to obtain a homogeneous mixture. Homogeneous glass spheres (diameter ~ 2.5-3 mm) were then produced at the Institut de Physique du Globe de Paris (IPGP), France, by fusing and quenching powder mixtures in an aerodynamic levitation laser furnace under different gas fluxes, employing gas mixes of Ar or $Ar+CO_2+H_2$ (Table S1). The resulting glass spheres were further polished into a cylindrical shape of 2 mm diameter and 1.5 mm length. Two glass cylinders (UM1, MM1) were encapsulated by a Re foil of 25 µm thickness (Table S1). An additional glass cylinder (UM2) was prepared with a double capsule design using Re foil of 25 µm thickness as inner capsule and Pt foil of 20 µm thickness as outer capsule material (Table S1). Two high pressure and high temperature syntheses (UM1, MM1) were performed in the Walker-type multi-anvil apparatus installed at IPGP at the conditions summarized in Table S1. 14/8 COMPRES assemblies were used, equipped with a graphite furnace, and with the capsule being inserted into a MgO sleeve and placed into the center of the assembly. The temperature was monitored with a D-type thermocouple inserted into a 4-hole alumina tube with the hot junction placed close to the capsule. One experiment (UM2) was conducted in the piston-cylinder apparatus at the IPGP using a ½'' assembly at 3 GPa and 1473 K (heating duration 24 h). The capsule surrounded by a MgO sleeve and MgO spacers was inserted into a cylindrical graphite furnace and talc sleeve which acted as pressure medium. The temperature was recorded with a S-type ($Pt_{90}Rh_{10}$-Pt_{100}) thermocouple with its hot junction placed near the capsule. All synthesis details are reported in Table S1.

S2. Samples' characterization

All recovered samples were well sintered and further analyzed by a set of electron microscopy techniques. Initial analyses have been conducted either using the Zeiss Ultra55 field emission scanning electron microscope (FE-SEM) at the IMPMC, Sorbonne

Université, France or JEOL JSM-7000F at the Geodynamics Research Center (GRC), Ehime University, Japan. All samples showed a homogenous grain distribution with a typical grain size of ~1-5 µm, and clear grain boundaries, typical of the so-called equilibrium texture (Figure S6). In order to analyze the compositions of all phases present in the individual experiments, samples UM2 and MM1 have been studied by electron microprobe (EMP), performing focused beam analyses at 15 kV, 10 nA using the Cameca SX-FIVE at Centre Camparis, Sorbonne Université. UM1 sample, showing grain sizes below ~1 µm, was thinned at IPGP by a Zeiss Auriga 40 focused ion beam (FIB) instrument (~50-100 nm thick slices) and analyzed at IMPMC using a JEOL 2100F transmission electron microscope (TEM) operating at 200 kV. Phase proportions of each sample were determined from the SEM and TEM images analyzing the greyscale histograms using the software ImageJ (individual greyscale maxima represent the different phases). Due to the technical difficulties of measuring Fe^{3+} vs. Fe^{2+} content of each of the very small phases present in our assembly by more direct methods (e.g., Mössbauer spectroscopy), the valence states of iron in Py, Gt and Mag were estimated by charge balance method (Quinn et al., 2016) using TEM/EMP data (Table 1). This approach has been proven to be a suitable method to determine $Fe^{3+}/\Sigma Fe$ when Mössbauer spectroscopy or other comparable techniques are not practical, with specific applications to garnets (Quinn et al., 2016). The main uncertainties of this method derive from the composition determination, especially from Si, as Si^{4+} is the most abundant cation and has the highest charge. Accordingly small uncertainties are expected for magnetite and garnet.

Major element composition of each sample was measured on a Zeiss Auriga 40 FEG-SEM equipped with a Bruker EDXS detector. Quantification was done using the K-lines of Fe, Mg, Al, Si, Ca, and O was obtained by stoichiometry, using the PhiRhoZ routine with pre-loaded standards. Large window scans (200 x 200 µm) were performed over multiple areas of the sample to show homogeneity and estimate analytical uncertainties (Table 1, method 1). The bulk composition of each sample was also assessed from the phase proportions and compositions of each phase (Table 1, method 2). Mineral compositions and phase proportions were checked before and/or after synchrotron measurements (see below). All compositions and phase proportions are reported in Table 1.

S3. In situ synchrotron experiments

Sound wave velocity and density measurements were performed at BL04B1, SPring-8, Japan. Three in situ experiments using combined ultrasonic interferometry, X-ray radiography and X-ray diffraction were carried out under high-pressure and high-temperature conditions in the DIA-type 1500 tons multi-anvil apparatus (SPEED1500), equipped with eight cubic tungsten carbide (WC) anvils. The high-quality samples were carefully polished at GRC to a thickness of 1.0 mm maintaining parallel and mirror-quality surfaces using ~0.5 μm diamond-coated polishing tools. The samples were surrounded by a MgO sleeve and placed in a modified 14/8 Co-doped MgO octahedron serving as pressure medium, equipped with a cylindrical Re foil heater. Two 2 μm thick Au foils were placed at the top and bottom of the sample, which acted as sample length indicator as well as to enhance the bonding between the individual layers. An Al_2O_3 corundum buffer rod was placed on top of the sample being in direct contact with the WC anvil. A pre-pressed pellet of MgO + Au + BN was placed at the back of the sample to enhance hydrostatic conditions at high pressure and to serve as pressure sensor during the experiments. The temperature was monitored with a D-type ($W_{97}Re_3$-$W_{75}Re_{25}$) thermocouple, whose hot-junction was placed at the bottom of the pressure marker. At first, the press load was increased to reach the target pressure of the first heating cycle, then temperature was increased to either 1000 or 1200 K (MM1) or 900 K (UM1 and UM2) (see Table S4 for details) and kept stable for 30 minutes to 1 hour to release deviatoric stresses that might have developed during cold compression. Data were collected for decreasing temperature, from 1000 K or 1200 K (MM1) or 900 K (UM1 and UM2) down to 300 K in steps of 200-300 K. The press load was then further increased and the overall procedure was repeated for three subsequent cycles (Figure S1). For ultrasonic measurements, a piezoelectric $LiNbO_3$ transducer was attached with a small amount of epoxy on a truncation of one WC anvil that was polished to mirror-quality. By applying alternating current, S- and P-waves were produced at the resonance frequencies of 40 and 60 MHz, respectively. A typical P-wave signal at high pressure and temperature can be seen in Figure S2. The variation in sample length at different pressure and temperature conditions was measured by imaging the two Au foils placed at both ends of the sample using X-ray radiography (Figure S3). Radiographs were

recorded using a high-resolution CCD camera (C11440, Hamamatsu Photonics, Iwata, Japan) with 1 pixel resolution corresponding to ~1.47 µm. Energy-dispersive diffraction patterns between 0 and 145 keV were collected both for the sample and pressure marker on an SSD detector at a fixed 2θ angle of ~ 6°, which was calibrated with the unit-cell volume of Au in the pressure marker before compressing each experiment. An example of a representative XRD pattern for UM1 collected at 5.5(1) GPa and 900 K is shown in Figure S5.

S4. Data analysis

The unit-cell volumes of the Au pressure marker were used to determine the pressure at each temperature point according to the *P-V-T* equation of state (Tsuchiya, 2003). The unit-cell parameters of olivine, orthopyroxene, garnet and, when possible, magnetite (Table S2) were determined using full profile LeBail refinements within the GSAS software package in the EXPGUI interface (Toby, 2001; Larson & Von Dreele, 2004). The densities (ρ) of the phase assemblage were then calculated according to the phase proportions obtained from SEM/TEM images and the volumes measured by XRD. The unit-cell volumes of magnetite could be clearly determined by XRD only for sample UM1 and not for sample UM2 due to the low amount of magnetite present in the phase assemblages (3 vol.%). In this latter case, the volumes at specific pressures and temperatures were calculated using the thermal equation of state proposed for $MgFe_2O_4$ by Levy et al., (2004), due to the missing thermal expansion information of the end-member magnetite (Fe_3O_4) at high pressures.

V_p and v_S were calculated according $v = \frac{2L}{t}$ with L representing the sample length obtained from X-ray radiography and t being the two-way travel time taken from ultrasonic data at each pressure and temperature condition measured during the experiments. The *P-T-* $v_{P,S}$ data was then fitted following the equation $v_{P,S} = v_{0P,S} + \partial(v_{P,S})/\partial P * P + \partial(v_{P,S})/\partial T * (T - 300K)$ in order to get the pressure and temperature dependence of each mineralogical assemblage (see Figure S4).

S5. Bulk density, bulk and shear moduli

The room temperature bulk densities for each experiment versus pressure are shown in Figure S9. For the upper mantle experiments UM1 and UM2, the larger density of UM1 reflects the higher abundance of magnetite (6 vol.%) in this phase assemblage relative to UM2 (3 vol.%). Similar to the wave velocities, the bulk density at ambient temperature of the mid-mantle experiment MM1 follows a smooth transition from the bulk densities of the upper mantle assemblages. The evolution of the bulk density at constant mineralogy along the areotherm case 12 is shown in Figure S10. Similar to the wave velocities, an initial decrease in densities can be observed due to the larger temperature effect relative to the pressure effect. Compared to thermodynamic end-member models calculated with Perple_X, which however are not for a constant mineralogy but for a mineralogy evolving along the areotherm, the bulk densities are comparable to the experimentally determined densities, although their phase assemblages containing olivine, pyroxene and garnet differ quite significantly depending on the bulk starting composition.

With knowledge of both bulk density and wave velocities, it is possible to calculate the bulk and shear moduli K_S and G following:

$$v_P = \sqrt{\frac{K_S + \frac{4}{3}G}{\rho}} \text{ and } v_S = \sqrt{\frac{G}{\rho}}.$$

Both K_S and G are shown in Figure S11 versus depth along the thin crust areotherm case 12 and are compared to self-consistent thermodynamic models. The elastic moduli clearly reflect the presence of magnetite and Fe^{3+}-rich garnet in the experimental phase assemblages, leading to lower bulk and shear moduli compared to the self-consistent thermodynamic models, and hence indicate slower wave velocities (Figure 3a). The availability of only Mg- or Fe^{2+} end-member data does not allow the direct comparison of thermodynamic models and experiments for the same mineralogy.

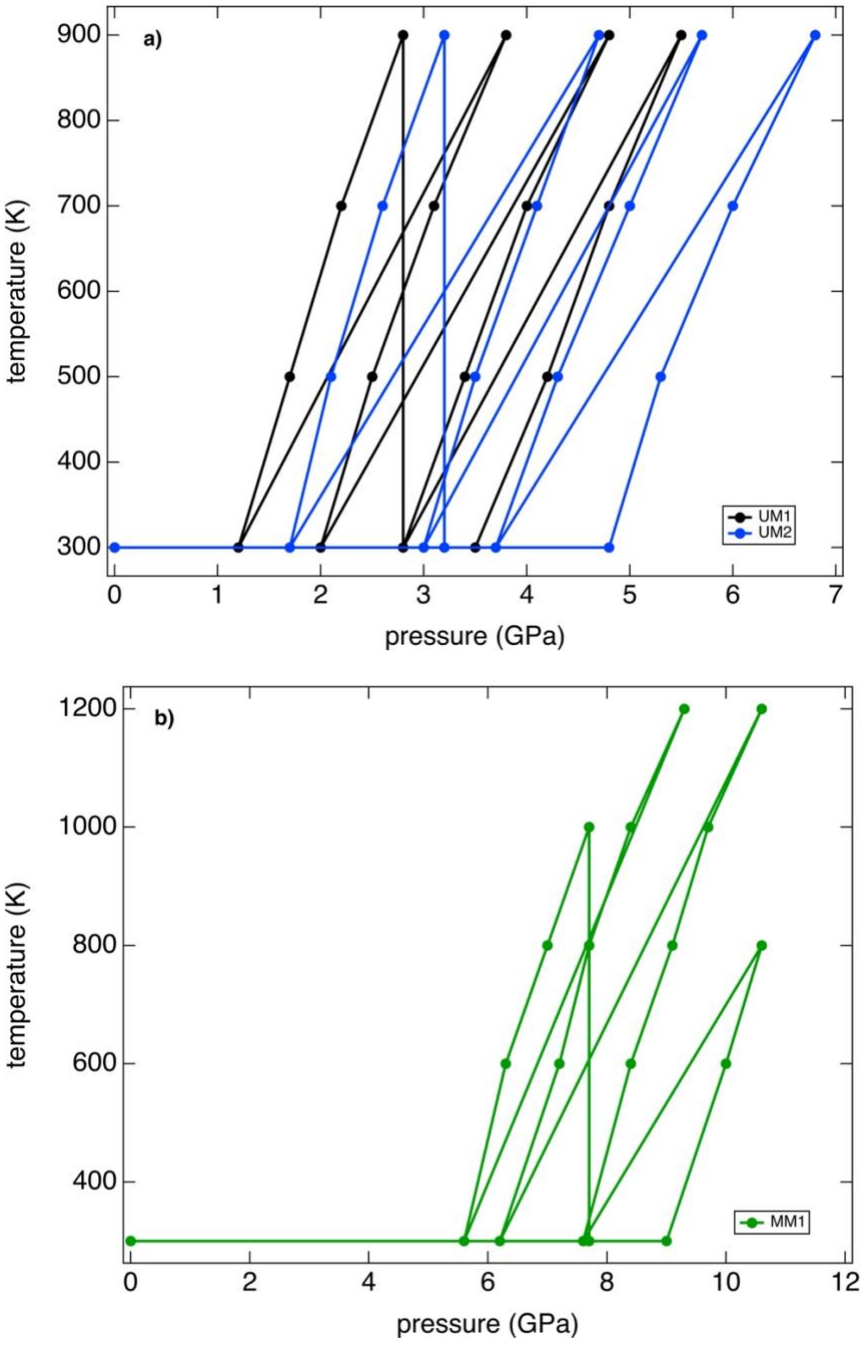

Figure S1. *P-T* path of the three in situ ultrasonic interferometry and diffraction experiments at BL04B1, SPring-8, Japan. The upper mantle experiments UM1 and UM2 (a) were first compressed to target pressure before increasing the temperature to 900 K in

four subsequent cycles. The same procedure was applied for the mid-mantle experiment MM1 (b) with the maximum temperature reached being 1200 K.

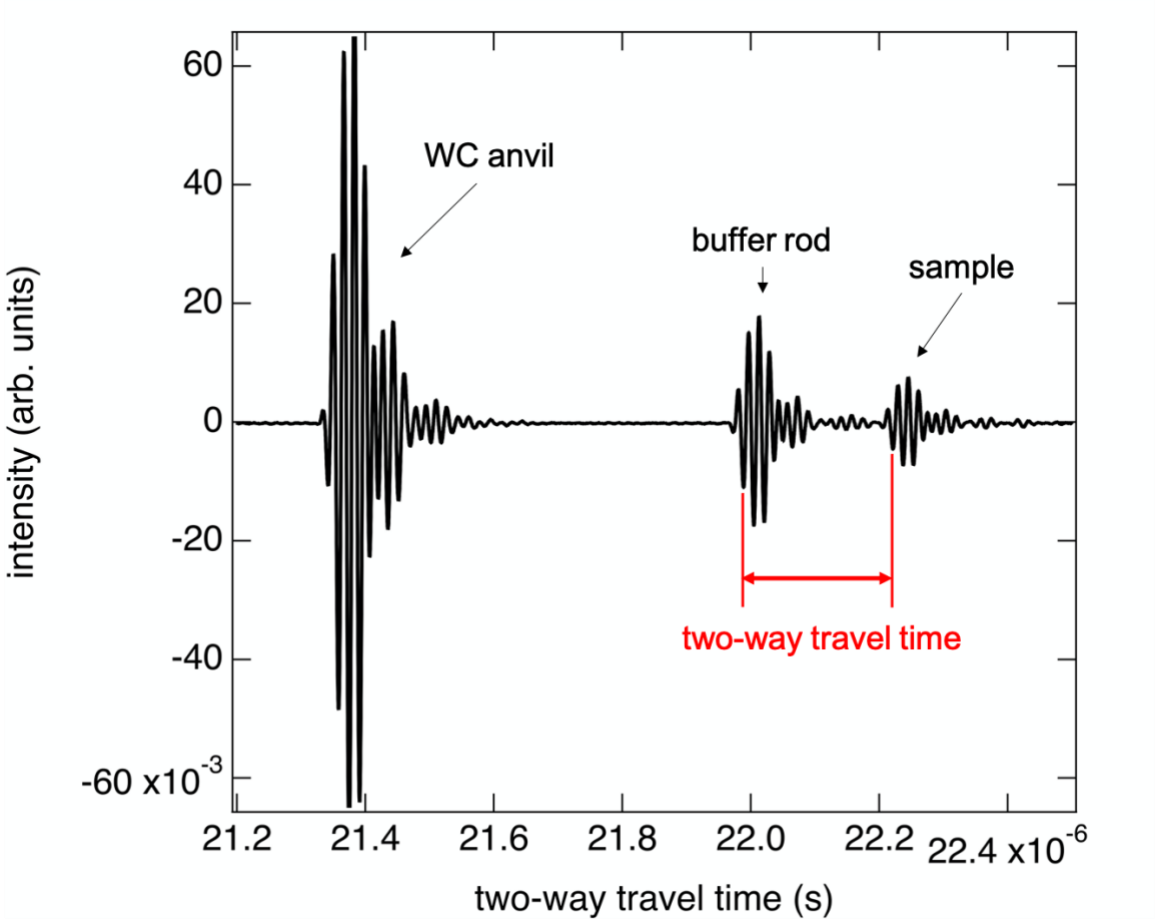

Figure S2. Representative ultrasonic signal collected for MM1 at 7.9 GPa and 1000 K.

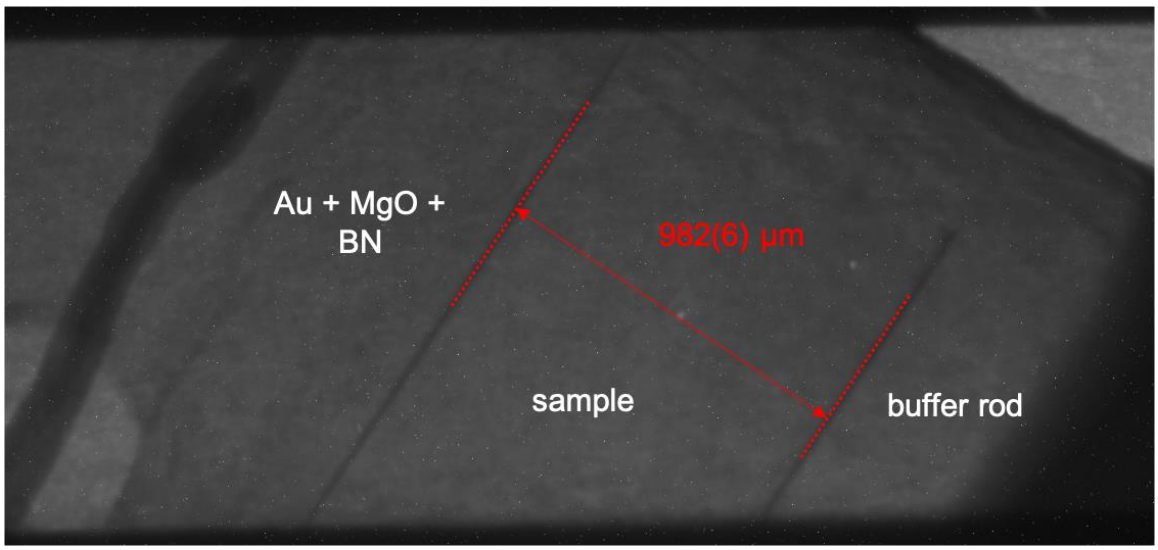

Figure S3. X-ray radiography image collected on MM1 at 7.9 GPa and 1000 K. By measuring the distance between the two gold foils, the sample length at each individual pressure and temperature point can be determined.

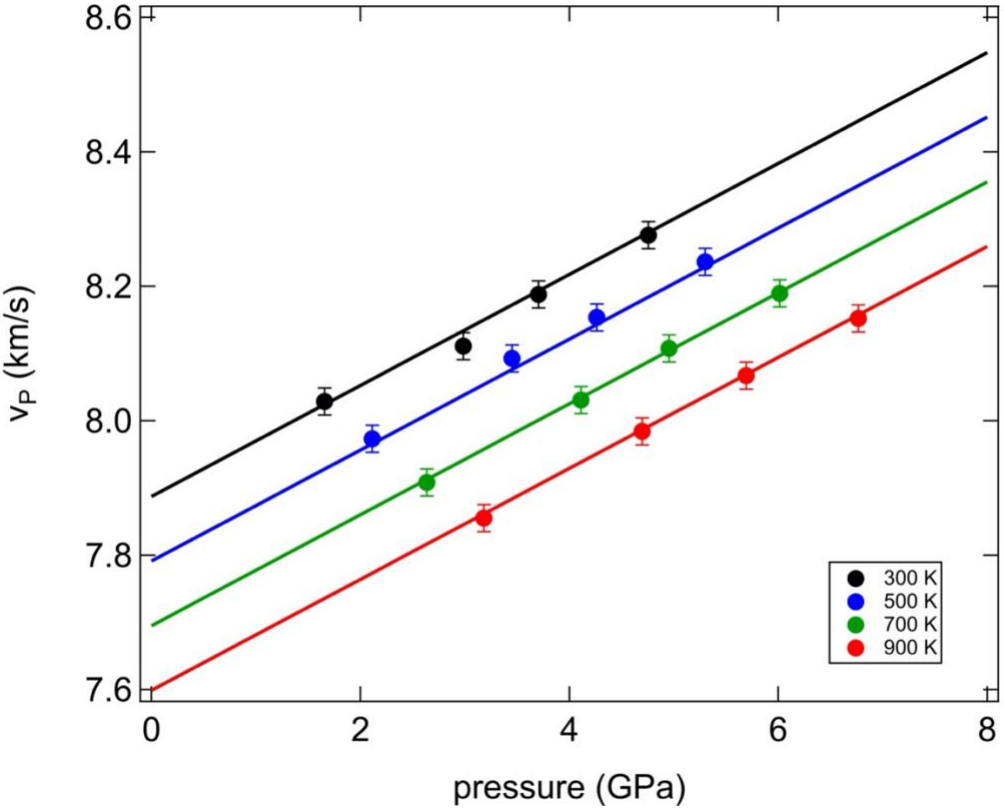
8.6
8.4
8.2
8.0
7.8
7.6
v_P (km/s)
0
2
4
6
8
pressure (GPa)
300 K
500 K
700 K
900 K

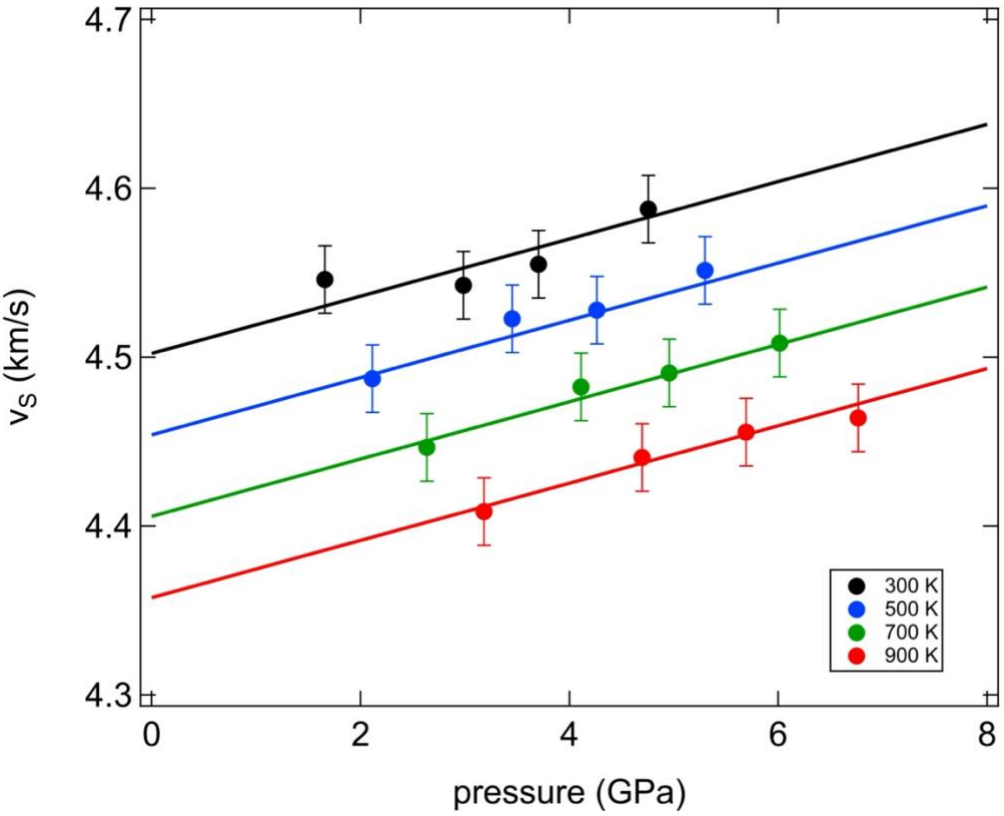
4.7
4.6
4.5
4.4
4.3
v_S (km/s)
0
2
4
6
8
pressure (GPa)
300 K
500 K
700 K
900 K

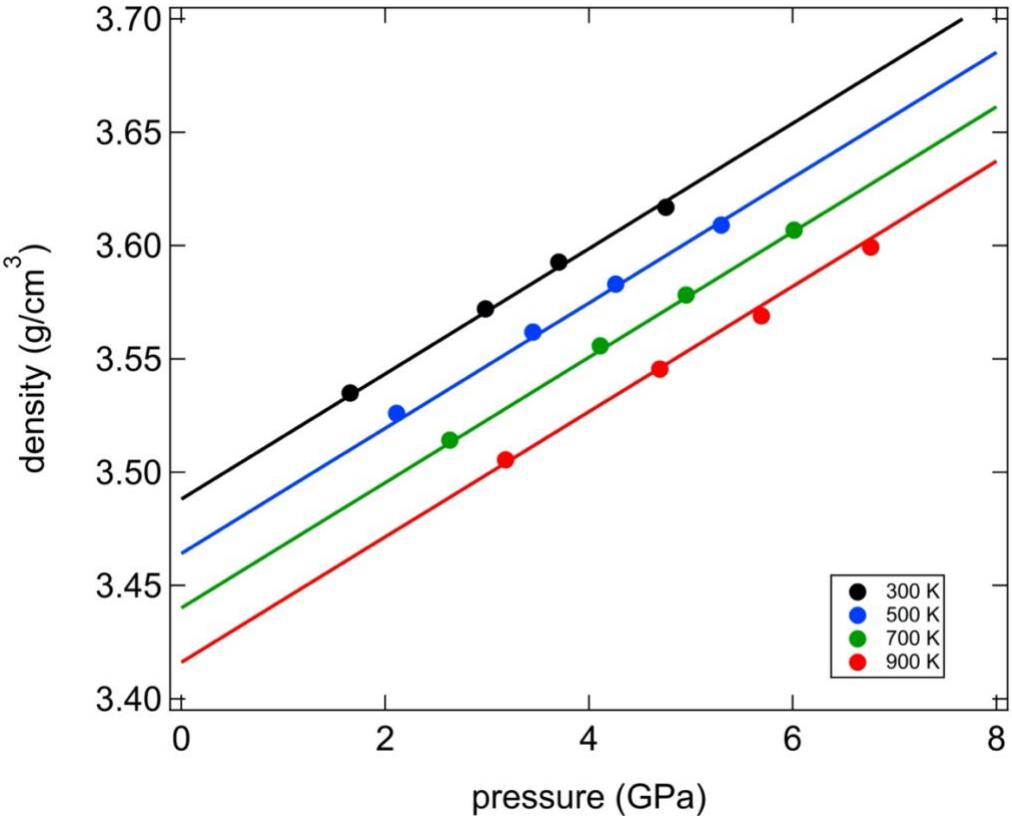

Figure S4. Wave velocities v_P (a), v_S (b) and bulk density (c) versus pressure collected along isotherms for the upper mantle experiment UM2. When not visible, propagated uncertainties are smaller than the symbols. A linear fitting procedure allows the determination of the pressure and temperature dependence of v_P, v_S and the bulk density.

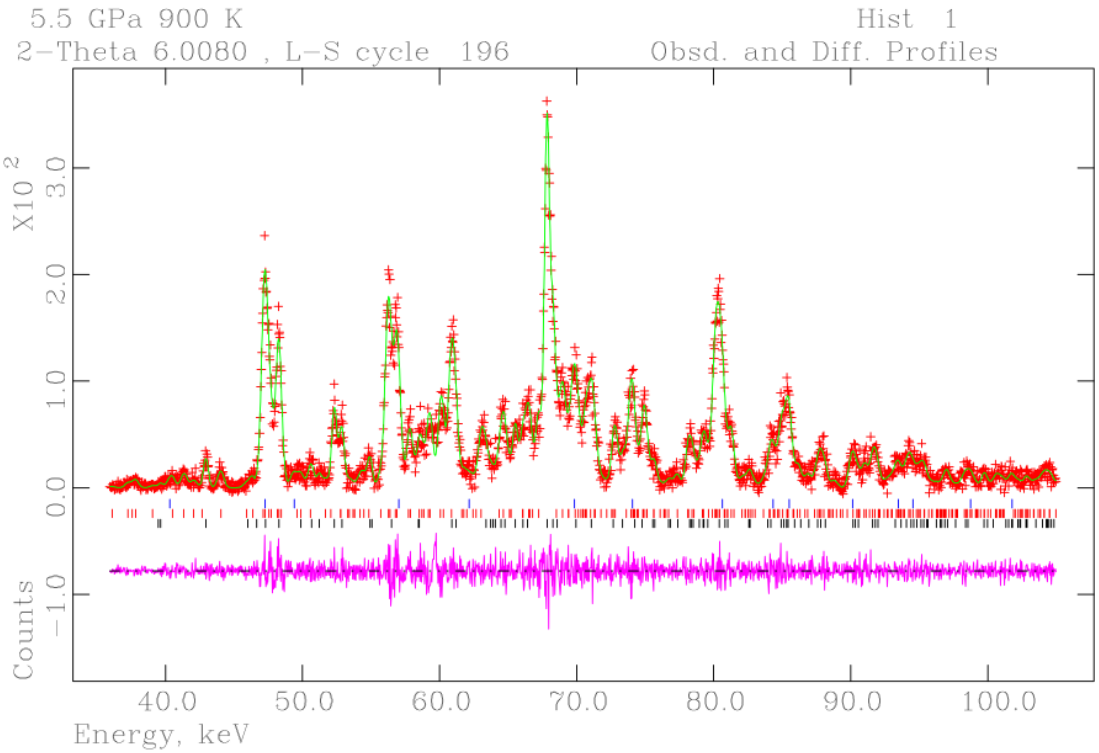

Figure S5. Representative energy-dispersive X-ray diffraction pattern collected for the upper mantle experiment UM1 at 5.5(1) GPa and 900 K. Blue thick marks correspond to indexed reflections of magnetite, red thick marks to orthopyroxene and black thick marks to olivine.

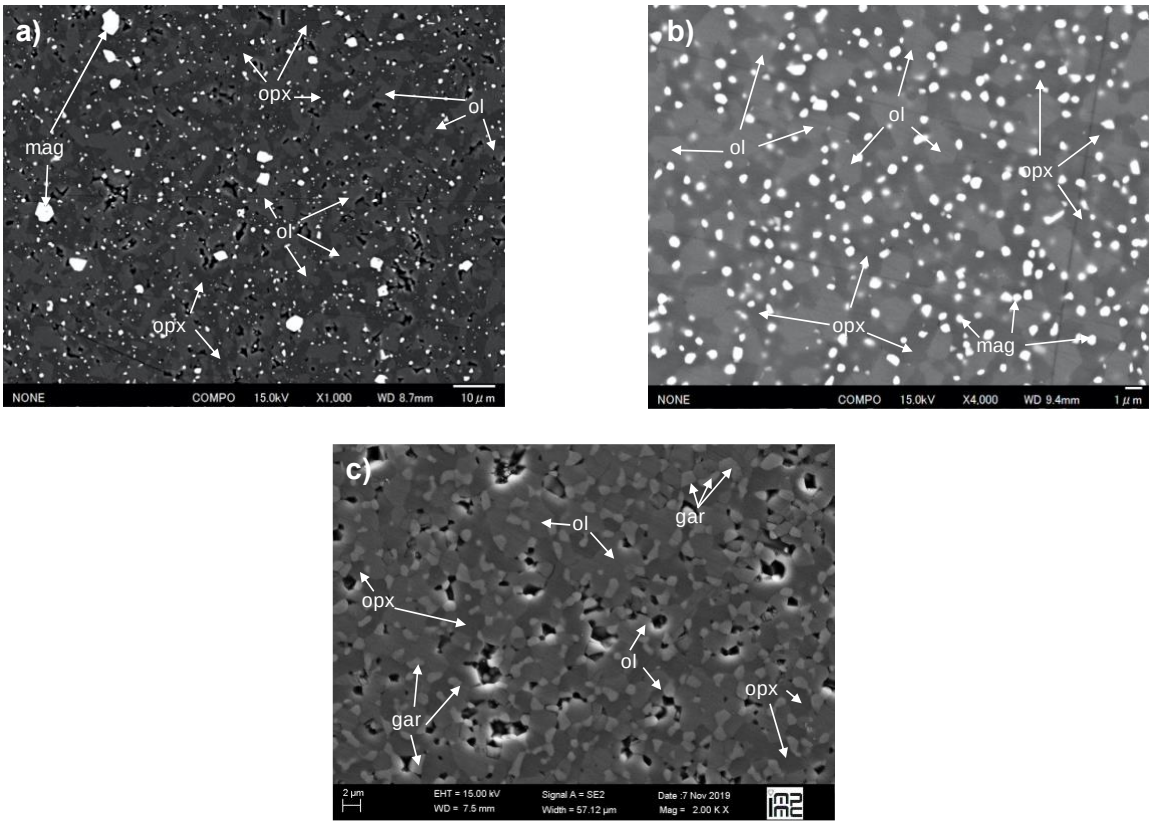

Figure S6. Backscattered electron images for the three mineralogical assemblages investigated in this study collected on the samples recovered after the ultrasonic experiments. The upper mantle experiment UM2 (a) and UM1 (b) contain a mixture of olivine (ol), orthopyroxene (opx) and magnetite (mag). The mid-mantle phase assemblage MM1 contains olivine, orthopyroxene and garnet (gar). The black areas in a) and c) are voids in the samples formed during sample preparation for SEM analyses and were not present during the high pressure and temperature ultrasonic experiments.

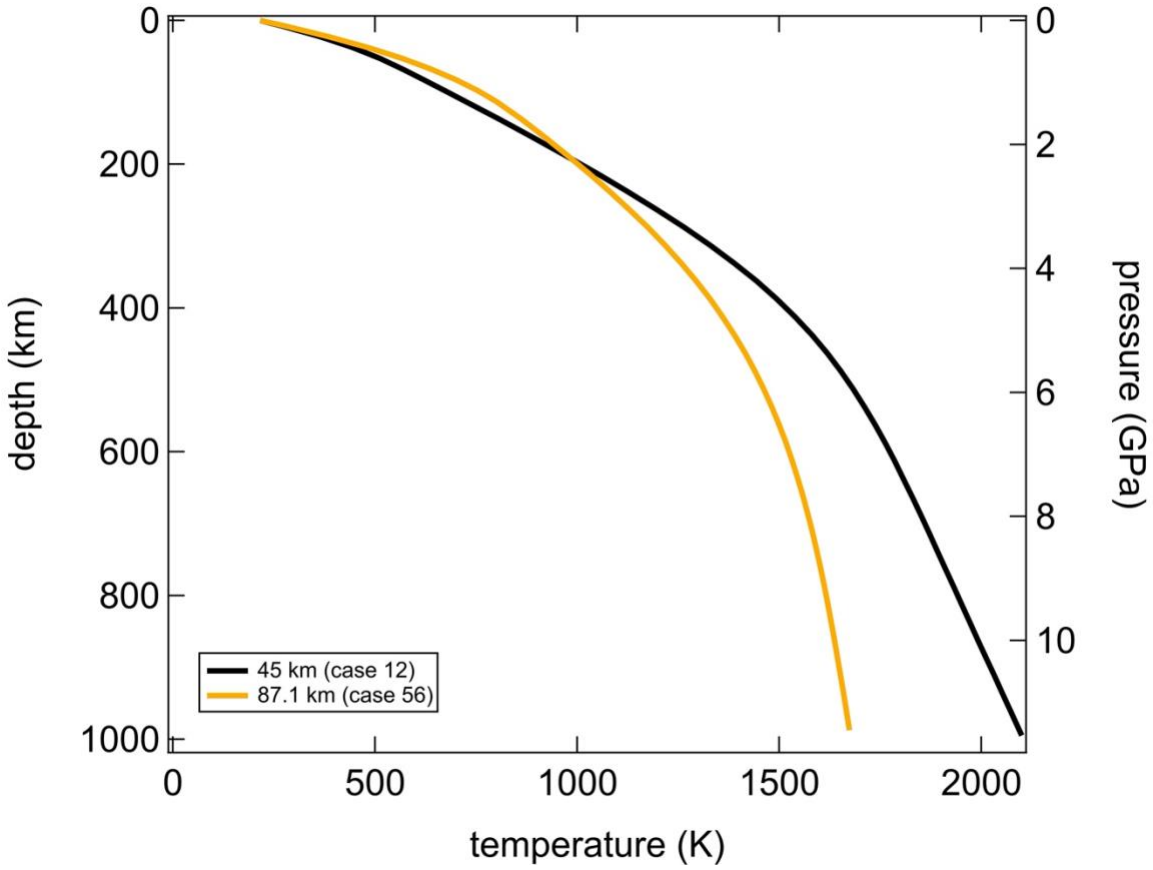

Figure S7. Two representative areotherms, case 12 (black) and case 56 (orange) for the Martian mantle used in this study. Both areotherms are part of a set of temperature profiles that were obtained from 3-D thermal evolution models as discussed in Plesa et al. (2018).

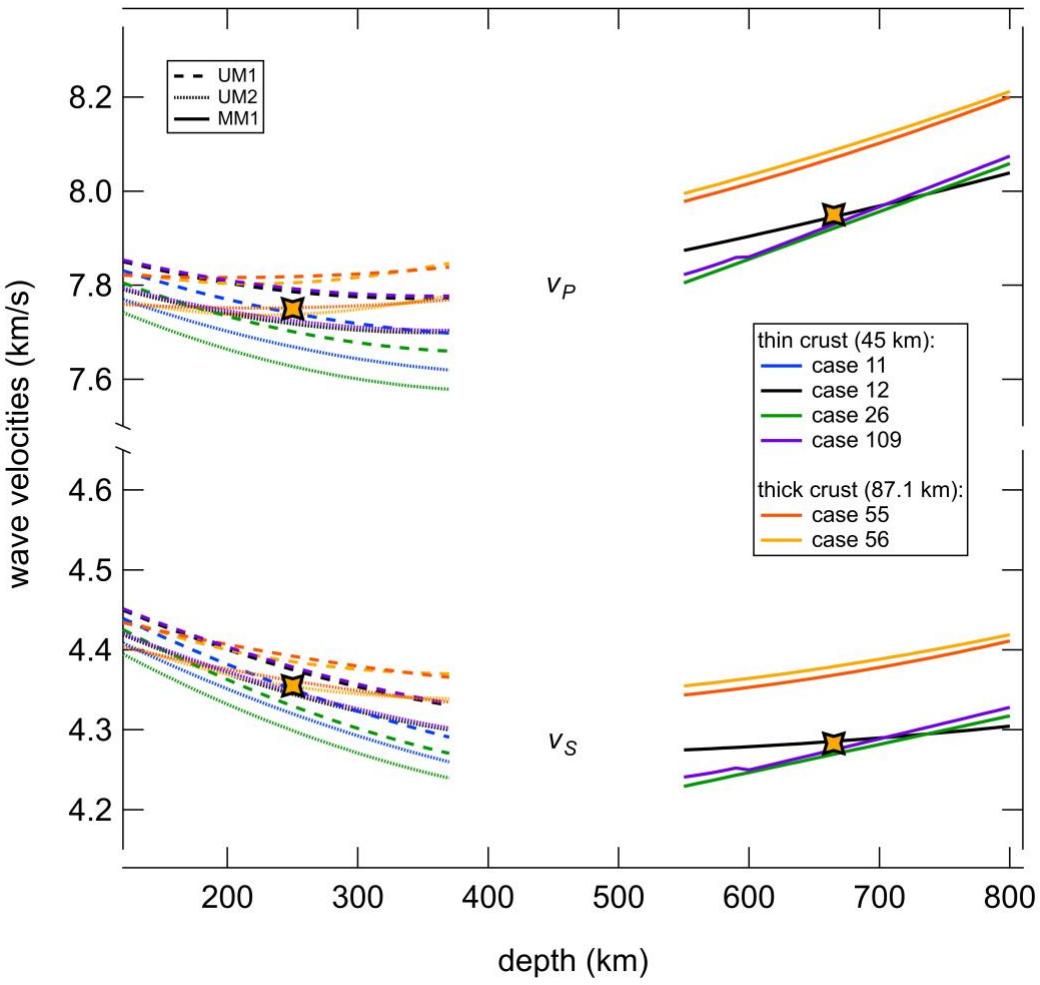

Figure S8. Wave velocities v_P and v_S as a function of depth along six areotherms representative for Mars. The areotherms consider different mantle rheologies, core radii and crustal thicknesses. The present-day crustal heat production rate is similar to the average value derived from the surface abundances of heat producing elements. Cases 11, 12, 26 and 109 are for thin crust areotherms (45 km average crustal thickness) and cases 55 and 56 are for thick crust areotherms (87.1 km average crustal thickness) (Plesa et al., 2018). Thin crust areotherms show low-velocity zones for both v_P and v_S whereas the thick crust areotherms only show low velocity zones for v_S.

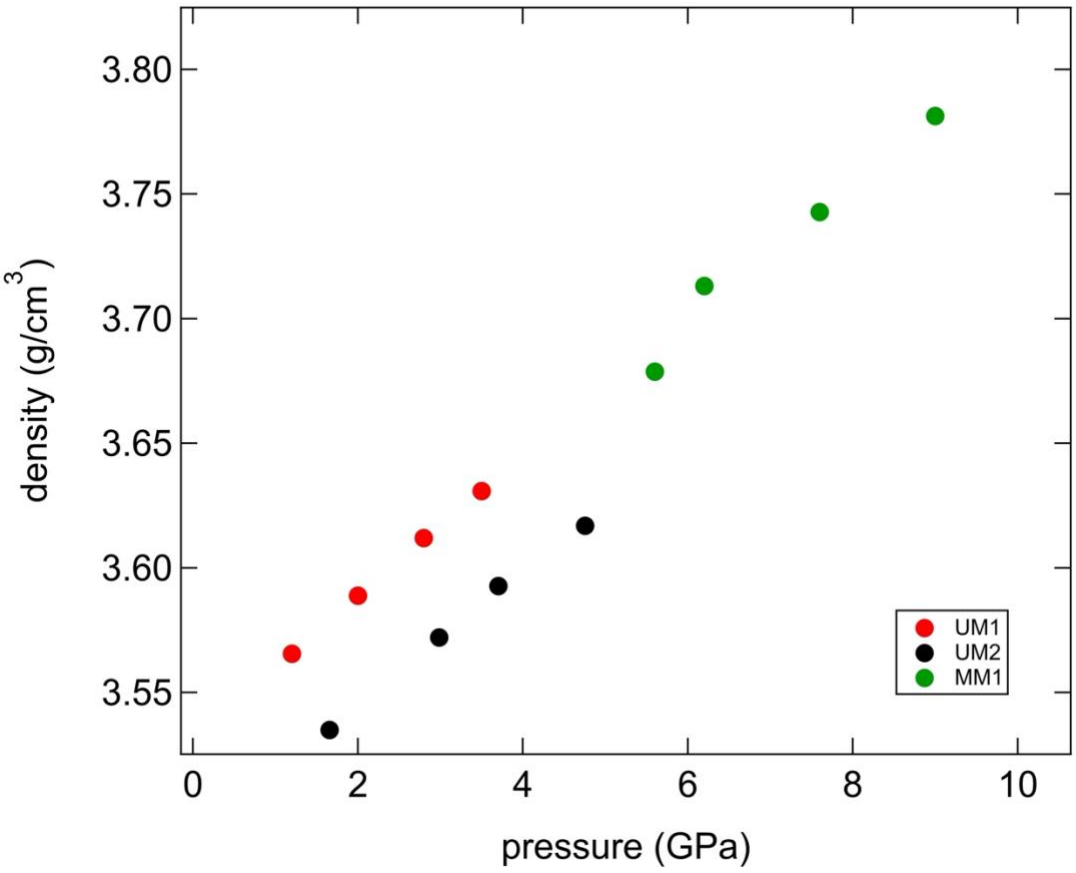

Figure S9. Bulk density of studied mineralogical assemblages versus pressure at 300 K.

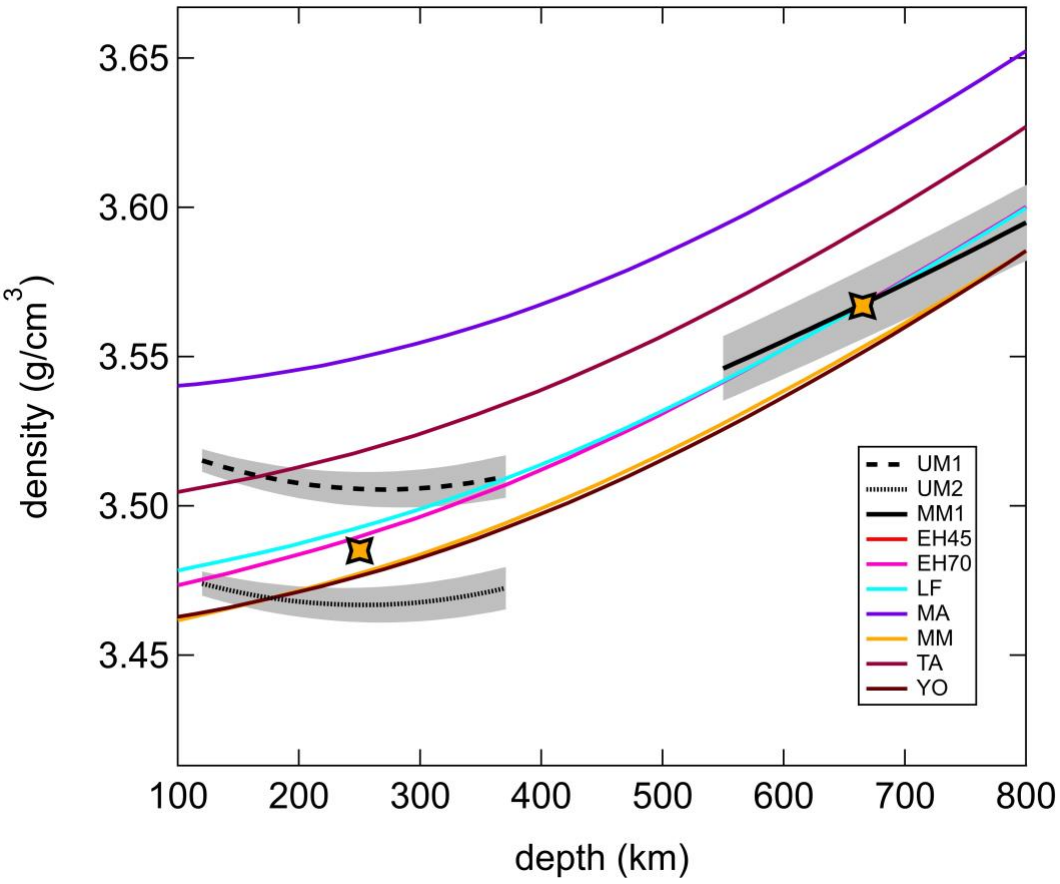

Figure S10. Bulk density of the three phase assemblages investigated in this study along the case 12 areotherm. For comparison, models based on thermodynamic end-member databases are plotted. N.B. experimental densities are for constant mineralogy (equilibrated at depth corresponding to either ~250 km or ~650-680 km), while models are for mineralogy changing with depth.

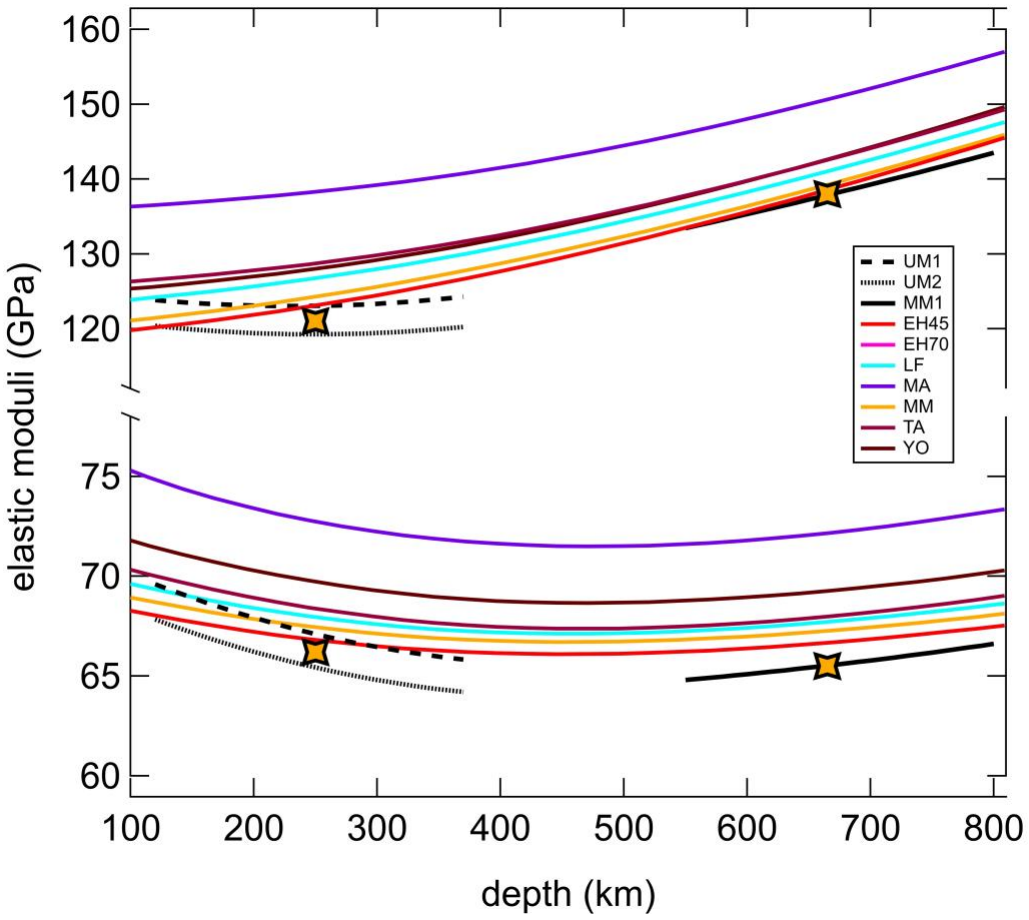

Figure S11. Bulk modulus K_S and shear modulus G for the three bulk assemblages studied versus depth. For comparison, the elastic moduli calculated from the self-consistent thermodynamic models are shown.

Table S1. Experimental conditions and run products of all synthesis experiments.

Run	Gas[a]	Capsule	P (GPa)	T (K)	Time (hr)	Product[b]	Grain size (μm)
UM1	Ar	Re	3	1373	1	Ol, Py, Mag	1-2
UM2	Ar+CO_2+H_2	Re+Pt	3	1473	24	Ol, Py, Mag	2-5
MM1	Ar	Re	8	1473	23	Ol, Py, Gt	1-3

[a] The gas flux used in aerodynamic levitation laser furnace for making glass.
[b] Run products are Ol, olivine; Py, pyroxene; Mag, magnetite; Gt, garnet.

Table S2. Unit-cell lattice parameters and densities of all phases present in the three mineralogical assemblages studied using energy-dispersive X-ray diffraction.

P (GPa)	*T* (K)	Ol					Py					Gt/Mag		
		a (Å)	*b* (Å)	c(Å)	*V* (Å^3)	*ρ* (g/cm^3)	*a* (Å)	*b* (Å)	*c* (Å)	*V* (Å^3)	*ρ* (g/cm^3)	*a* (Å)	*V* (Å^3)	*ρ* (g/cm^3)
UM1 (Ol, Py, Mag)														
0.0001(1)	300	4.7743(4)	10.2407(9)	6.0074(4)	293.72(3)	3.5064(3)	18.2845(12)	8.8197(4)	5.2081(3)	839.88(6)	3.4960(3)	8.3450(4)	581.13(8)	4.7878(6)
2.76(2)	900	4.7694(6)	10.2206(16)	6.0064(7)	292.79(5)	3.5176(5)	18.2728(24)	8.8087(9)	5.1946(6)	836.12(13)	3.4113(5)	8.3579(8)	583.84(16)	4.7656(13)
2.23(3)	700	4.7631(7)	10.2159(24)	6.0031(8)	292.11(6)	3.5257(7)	18.2519(23)	8.7966(8)	5.1923(6)	833.64(12)	3.4214(5)	8.3480(5)	581.77(11)	4.7825(9)
1.68(4)	500	4.7586(7)	10.2088(19)	5.9968(8)	291.32(5)	3.5352(6)	18.2263(22)	8.7907(9)	5.1851(6)	830.76(12)	3.4332(5)	8.3322(5)	578.47(10)	4.8098(8)
1.19(8)	300	4.7534(7)	10.2014(21)	5.9899(8)	290.46(6)	3.5457(7)	18.2236(21)	8.7839(8)	5.1809(6)	829.33(11)	3.4392(5)	8.3217(4)	576.29(9)	4.8280(8)
3.79(5)	900	4.7599(6)	10.2081(21)	5.9932(8)	291.21(6)	3.5366(7)	18.2159(21)	8.7834(8)	5.1828(6)	829.23(12)	3.4396(5)	8.3378(5)	579.63(10)	4.8002(9)
3.10(7)	700	4.7559(5)	10.1929(18)	5.9856(7)	290.16(5)	3.5494(6)	18.2126(18)	8.7749(7)	5.1776(5)	827.45(10)	3.4470(4)	8.3261(4)	577.21(8)	4.8203(7)
2.48(8)	500	4.7532(6)	10.1817(19)	5.9779(8)	289.31(5)	3.5599(6)	18.2024(18)	8.7693(7)	5.1703(5)	825.30(10)	3.4560(4)	8.3119(4)	574.26(9)	4.8451(7)
2.02(15)	300	4.7497(7)	10.1804(23)	5.9699(9)	288.67(6)	3.5677(7)	18.1761(19)	8.7659(8)	5.1690(5)	823.57(10)	3.4632(4)	8.3045(5)	572.72(10)	4.8581(8)
4.76(10)	900	4.7523(7)	10.1695(23)	5.9781(10)	288.91(6)	3.5647(8)	18.1865(20)	8.7568(9)	5.1664(6)	822.77(12)	3.4666(5)	8.3197(5)	575.88(10)	4.8315(8)
4.01(5)	700	4.7506(7)	10.1648(20)	5.9712(8)	288.34(5)	3.5718(7)	18.1727(20)	8.7534(8)	5.1646(5)	821.54(11)	3.4718(5)	8.3099(5)	573.84(10)	4.8486(8)
3.36(8)	500	4.7458(6)	10.1525(18)	5.9685(8)	287.57(5)	3.5852(6)	18.1600(19)	8.7441(8)	5.1605(6)	819.45(11)	3.4806(5)	8.2991(5)	571.59(9)	4.8677(8)
2.78(5)	300	4.7423(7)	10.1471(21)	5.9603(9)	286.81(6)	3.5908(7)	18.1592(19)	8.7400(8)	5.1562(6)	818.34(11)	3.4853(5)	8.2868(5)	569.06(10)	4.8894(8)
5.54(4)	900	4.7440(7)	10.1478(18)	5.9670(8)	287.26(5)	3.5852(6)	18.1626(18)	8.7336(8)	5.1565(5)	817.95(11)	3.4870(5)	8.3037(5)	572.55(10)	4.8595(9)
4.83(3)	700	4.7438(7)	10.1312(18)	5.9603(8)	286.45(5)	3.5953(6)	18.1400(19)	8.7286(8)	5.1550(6)	816.23(11)	3.4944(5)	8.2980(5)	571.38(10)	4.8695(8)
4.19(6)	500	4.7383(7)	10.1301(20)	5.9577(8)	285.96(5)	3.6015(7)	18.1318(18)	8.7256(8)	5.1505(6)	814.88(11)	3.5002(5)	8.2861(5)	568.91(9)	4.8906(8)
3.55(3)	300	4.7373(6)	10.1254(18)	5.9506(8)	285.44(5)	3.6081(6)	18.1255(19)	8.7190(8)	5.1475(6)	813.49(11)	3.061(5)	8.2763(5)	566.91(9)	4.9079(8)
UM2 (Ol, Py, Mag)														
0.0001(1)	300	4.7789(3)	10.2510(8)	6.0123(4)	294.54(2)	3.4950(2)	18.2725(11)	8.8167(4)	5.2125(3)	839.75(6)	3.3982(2)			4.5269[a]
3.18(11)	900	4.7675(4)	10.2208(10)	6.0043(5)	292.58(3)	3.5184(4)	18.2324(26)	8.7878(9)	5.1987(6)	832.96(12)	3.4259(5)			4.5701 [a]

2.64(10)	700	4.7622(4)	10.2065(11)	6.0000(5)	291.63(3)	3.5299(4)	18.2182(27)	8.7872(9)	5.1938(6)	831.46(12)	3.4321(5)				4.5683 [a]
2.11(12)	500	4.7584(4)	10.1962(10)	5.9888(5)	290.56(3)	3.5428(3)	18.2109(23)	8.7773(8)	5.1847(5)	828.73(11)	3.4434(4)				4.5676 [a]
1.66(9)	300	4.7521(3)	10.1882(9)	5.9839(5)	289.71(3)	3.5532(3)	18.1882(25)	8.7745(8)	5.1810(6)	826.84(12)	3.4513(5)				4.5683 [a]
4.70(6)	900	4.7554(4)	10.1685(10)	5.9822(5)	289.27(3)	3.5587(4)	18.1930(25)	8.7579(11)	5.1668(6)	823.24(13)	3.4663(5)				4.6035 [a]
4.11(9)	700	4.7518(4)	10.1561(12)	5.9744(5)	288.32(3)	3.5703(4)	18.1858(27)	8.7437(11)	5.1630(8)	820.96(14)	3.4760(6)				4.6023 [a]
3.45(12)	500	4.7440(4)	10.1545(12)	5.9746(5)	287.81(3)	3.5767(4)	18.1612(21)	8.7419(10)	5.1617(6)	819.49(12)	3.4822(5)				4.5999 [a]
2.99(14)	300	4.7417(3)	10.1441(10)	5.9655(5)	286.94(3)	3.5875(4)	18.1618(23)	8.7284(10)	5.1540(6)	817.03(12)	3.4927(5)				4.5986 [a]
5.69(7)	900	4.7448(4)	10.1432(9)	5.9737(6)	287.50(3)	3.5805(4)	18.1459(24)	8.7290(11)	5.1590(6)	817.17(13)	3.4921(6)				4.6251 [a]
4.96(5)	700	4.7419(4)	10.1341(9)	5.9655(5)	286.67(3)	3.5909(4)	18.1517(21)	8.7189(9)	5.1505(6)	815.13(12)	3.5008(5)				4.6221 [a]
4.26(5)	500	4.7407(4)	10.1300(10)	5.9601(5)	286.22(3)	3.5965(4)	18.1307(19)	8.7185(8)	5.1502(5)	814.10(11)	3.5053(5)				4.6178 [a]
3.70(9)	300	4.7384(4)	10.1207(9)	5.9533(5)	285.50(3)	3.6057(4)	18.1345(18)	8.7045(9)	5.1404(5)	811.42(10)	3.5169(5)				4.6146 [a]
6.77(8)	900	4.7343(4)	10.1137(8)	5.9530(5)	285.03(3)	3.6115(4)	18.1423(25)	8.6919(9)	5.1378(7)	810.18(14)	3.5223(6)				4.6483 [a]
6.01(9)	700	4.7331(4)	10.1040(8)	5.9474(5)	284.42(3)	3.6193(4)	18.1242(21)	8.6896(9)	5.1325(6)	808.33(12)	3.5303(5)				4.6436 [a]
5.30(10)	500	4.7316(4)	10.1021(8)	5.9453(5)	284.18(3)	3.6224(4)	18.1165(21)	8.6875(8)	5.1334(7)	807.93(12)	3.5321(5)				4.6397 [a]
4.76(9)	300	4.7302(4)	10.0929(9)	5.9380(5)	283.49(3)	3.6312(4)	18.1058(19)	8.6800(8)	5.1303(6)	806.27(11)	3.5393(5)				4.6391 [a]
MM1 (Ol, Py, Gt)															
0.0001(1)	300	4.7787(2)	10.2436(6)	6.0079(3)	294.09(2)	3.5145(2)	18.2864(23)	8.8281(9)	5.2051(5)	840.29(11)	3.3836(4)	11.6416(3)	1577.77(11)	3.8533(3)	
7.69(3)	1000	4.7397(4)	10.0913(8)	5.9516(3)	284.67(3)	3.6309(3)	18.5791(46)	8.6969(13)	5.0787(13)	820.62(21)	3.4647(9)	11.5443(5)	1538.52(18)	3.9516(5)	
7.02(10)	800	4.7355(4)	10.0840(6)	5.9458(4)	283.93(2)	3.6404(3)	18.6685(43)	8.6850(13)	5.0419(14)	817.48(22)	3.4780(9)	11.5365(4)	1535.41(18)	3.9596(5)	
6.34(10)	600	4.7320(4)	10.0771(7)	5.9399(4)	283.25(3)	3.6491(3)	18.6448(53)	8.6741(16)	5.0523(13)	817.09(21)	3.4797(9)	11.5260(4)	1531.21(17)	3.9705(4)	
5.58(10)	300	4.7276(4)	10.0699(6)	5.9333(4)	282.47(2)	3.6592(3)	18.6353(66)	8.6812(16)	5.0727(10)	820.65(28)	3.4646(12)	11.5118(4)	1525.58(17)	3.9851(4)	
9.26(6)	1200	4.7298(4)	10.0773(9)	5.9552(7)	283.85(3)	3.6414(4)	18.4676(34)	8.7101(10)	5.0821(10)	817.48(18)	3.4780(8)	11.5376(4)	1535.85(17)	3.9585(4)	
8.37(7)	1000	4.7333(3)	10.0593(10)	5.9405(5)	282.85(3)	3.6543(3)	18.4428(28)	8.7069(8)	5.0746(7)	814.88(13)	3.4891(6)	11.5233(4)	1530.14(16)	3.9733(4)	
7.73(6)	800	4.7301(4)	10.0543(10)	5.9334(5)	282.18(3)	3.6629(4)	18.4168(31)	8.7018(8)	5.0679(8)	812.18(14)	3.5007(6)	11.5128(4)	1525.94(15)	3.9842(4)	
7.16(7)	600	4.7263(4)	10.0533(9)	5.9262(5)	281.59(3)	3.6706(4)	18.3025(29)	8.7006(7)	5.0878(9)	810.19(14)	3.5093(6)	11.5041(4)	1522.49(17)	3.9932(5)	
6.23(7)	300	4.7223(3)	10.0420(9)	5.9155(5)	280.52(3)	3.6845(4)	18.1134(26)	8.6998(8)	5.1218(7)	807.10(13)	3.5228(5)	11.4902(4)	1517.01(16)	4.0077(4)	
10.57(6)	1200	4.7286(6)	10.0340(12)	5.9166(11)	280.72(4)	3.6819(5)	18.3059(24)	8.6974(9)	5.0616(8)	805.88(14)	3.5281(6)	11.4985(6)	1520.29(24)	3.9990(6)	
9.71(11)	1000	4.7247(5)	10.0295(10)	5.9149(7)	280.28(3)	3.6877(4)	18.2972(32)	8.6899(9)	5.0650(8)	805.34(15)	3.5304(7)	11.4908(6)	1517.23(24)	4.0071(6)	
9.09(9)	800	4.7232(5)	10.0252(11)	5.9041(8)	279.57(4)	3.6971(5)	18.2834(20)	8.6885(8)	5.0682(7)	805.11(13)	3.5314(6)	11.4828(5)	1514.07(20)	4.01549(5)	

8.42(8)	600	4.7183(3)	10.0134(8)	5.9051(5)	279.00(3)	3.7047(3)	18.2830(32)	8.6790(9)	5.0627(9)	803.33(16)	3.5393(7)	11.4709(5)	1509.36(18)	4.0280(5)
7.56(8)	300	4.7130(4)	10.0011(8)	5.8999(4)	278.09(3)	3.7168(3)	18.3443(39)	8.6689(13)	5.0384(8)	801.23(18)	3.5486(8)	11.4622(5)	1505.94(20)	4.0371(5)
10.58(9)	800	4.7060(5)	9.9792(9)	5.8972(8)	276.94(3)	3.7322(4)	18.2249(38)	8.6601(12)	5.0178(11)	791.95(20)	3.5901(9)	11.4492(5)	1500.81(20)	4.0509(5)
9.97(16)	600	4.7072(4)	9.9698(10)	5.8859(6)	276.22(3)	3.7419(4)	18.2332(24)	8.6510(10)	5.0176(9)	791.46(16)	3.5924(7)	11.4406(5)	1497.41(21)	4.0601(6)
9.03(13)	300	4.7037(4)	9.9653(9)	5.8808(6)	275.66(3)	3.7496(4)	18.2236(20)	8.6424(9)	5.0155(7)	789.91(13)	3.5994(6)	11.4295(4)	1493.06(18)	4.0719(5)

[a] The densities were calculated using the equation of state of magnesioferrite proposed by Levy et al., (2004).

Table S3. Experimentally observed phase proportion (in weight percent) in comparison with results obtained for the bulk composition of the starting material by Gibbs free energy minimization at the same pressure and temperature conditions. For completeness we also report the phase proportion at the same pressure experimentally obtained by Bertka & Fei (1997) for the Dreibus and Wänke (1985) bulk chemistry. Phases are olivine (Ol), orthopyroxene (Opx), clinopyroxene (Cpx), garnet (Gt) and magnetite (Mag).

Condition	Ol	Opx	Cpx	Gt	Mag	
This study [a]						
3 GPa, 1373K	43.1	48.9	- [b]		8.0	UM1
3 GPa, 1473K	43.3	52.8	-		3.9	UM2
8 GPa, 1473K	46.5	28.6	-	24.9		MM1
Modelling						
3 GPa, 1373K	51.7	32.0	4.7	11.6		
3 GPa, 1473K	51.7	34.1	3.4	10.8		
8 GPa, 1473K	51.8	28.2	5.6	14.4		
Bertka & Fei (1997) [c]						
3 GPa	58.4	18.9	12.8	9.9		
8 GPa	58.4	8.2	23.5	9.9		

[a] The weight percentage is derived from the volume percentage in Table 1 and the density of each phase at room pressure and 300 K in Table S2.
[b] Clinopyroxene, expected in our samples according to estimated bulk chemistry (Bulk (1)) and the bulk chemistry of the starting material (see Table 1), can't be detected in the SEM image and EMP composition point measurement due to its small grain size and amount.
[c] The phase proportion from Bertka & Fei (1997) (their Figure 8).

Table S4. Experimental pressure and temperature, compressional (v_P) and shear (v_S) wave velocities, and densities of measured samples.

P (GPa)	T (K)	v_P (km/s)	v_S (km/s)	ρ (g/cm^3)
UM1				
0.0001(1)	300			3.5244(3)
2.76(2)	900	7.88(1)	4.44(1)	3.5356(6)
2.23(3)	700	7.94(1)	4.48(1)	3.5451(6)
1.68(4)	500	7.99(1)	4.52(1)	3.5566(6)
1.19(8)	300	8.04(1)	4.55(1)	3.5655(6)
3.79(5)	900	7.97(1)	4.44(1)	3.5596(6)
3.10(7)	700	8.02(1)	4.49(1)	3.5704(5)

2.48(8)	500	8.07(1)	4.52(1)	3.5810(5)
2.02(15)	300	8.09(2)	4.55(1)	3.5888(6)
4.76(10)	900	8.05(2)	4.46(1)	3.5874(7)
4.01(5)	700	8.09(2)	4.50(1)	3.5941(6)
3.36(8)	500	8.11(2)	4.54(1)	3.6039(6)
2.78(5)	300	8.14(2)	4.58(1)	3.6119(6)
5.54(4)	900	8.11(2)	4.49(2)	3.6082(6)
4.83(3)	700	8.16(2)	4.53(2)	3.6171(6)
4.19(6)	500	8.19(2)	4.56(1)	3.6239(6)
3.55(3)	300	8.22(2)	4.61(2)	3.6308(6)

UM2

0.0001(1)	300			3.4796(2)
3.18(11)	900	7.85(2)	4.41(2)	3.5055(4)
2.64(10)	700	7.91(2)	4.45(2)	3.5142(4)
2.11(12)	500	7.97(2)	4.49(1)	3.5260(4)
1.66(9)	300	8.03(3)	4.55(3)	3.5350(4)
4.70(6)	900	7.98(2)	4.44(2)	3.5455(5)
4.11(9)	700	8.03(2)	4.48(2)	3.5558(5)
3.45(12)	500	8.09(2)	4.52(2)	3.5618(4)
2.99(14)	300	8.11(2)	4.54(2)	3.5721(4)
5.69(7)	900	8.07(2)	4.46(1)	3.5690(5)
4.96(5)	700	8.11(2)	4.49(1)	3.5782(4)
4.26(5)	500	8.15(2)	4.53(1)	3.5830(4)
3.70(9)	300	8.19(2)	4.56(2)	3.5927(4)
6.77(8)	900	8.15(2)	4.46(1)	3.5993(5)
6.01(9)	700	8.19(2)	4.51(2)	3.6068(5)
5.30(10)	500	8.24(2)	4.55(2)	3.6090(4)

MM1

0.0001(1)	300			3.5559(3)
7.69(3)	1000	8.36(2)	4.57(1)	3.6576(6)
7.02(10)	800	8.42(2)	4.63(2)	3.6678(6)
6.34(10)	600	8.46(2)	4.67(2)	3.6750(6)
5.58(10)	300	8.53(3)	4.74(3)	3.6787(7)
9.26(6)	1200	8.39(3)	4.55(3)	3.6680(5)
8.37(7)	1000	8.45(3)	4.62(3)	3.6808(4)
7.73(6)	800	8.50(3)	4.67(3)	3.6909(5)
7.16(7)	600	8.57(3)	4.73(3)	3.6992(5)
6.23(7)	300	8.64(2)	4.80(2)	3.7131(4)
10.57(6)	1200	8.56(3)	4.63(3)	3.7114(6)
9.71(11)	1000	8.60(3)	4.69(3)	3.7167(6)

9.09(9)	800	8.63(3)	4.72(3)	3.7234(5)
8.42(8)	600	8.70(2)	4.77(2)	3.7322(6)
7.56(8)	300	8.76(3)	4.83(3)	3.7428(6)
10.58(9)	800	8.75(3)	4.75(3)	3.7655(6)
9.97(16)	600	8.79(4)	4.79(4)	3.7729(6)
9.03(13)	300	8.85(4)	4.85(3)	3.7813(5)

Table S5. Results of 2-Dimensional global linear fitting for velocity and density

$\boldsymbol{M = M_0 + \partial M/\partial P * P + \partial M/\partial T * (T - 300\ K)}$ with M= {v_P, v_S, ρ}.

Sample	v_{P0} (km·s^{-1})	$\partial v_P/\partial P$ (km·s^{-1}·GPa^{-1})	$\partial v_P/\partial T$ (km·s^{-1}·K^{-1})	v_{S0} (km·s^{-1})	$\partial v_S/\partial P$ (km·s^{-1}·GPa^{-1})	$\partial v_S/\partial T$ (km·s^{-1}·K^{-1})	ρ_0 (g ·cm^{-3})	$\partial\rho/\partial P$ (g ·cm^{-3}·GPa^{-1})	$\partial\rho/\partial T$ (g ·cm^{-3}·K^{-1})
UM1	7.94(1)	0.080(3)	-0.00045(2)	4.53(1)	0.017(2)	-0.00024(1)	3.532(2)	0.0282(7)	-0.000128(4)
UM2	7.89(1)	0.083(2)	-0.00048(1)	4.50(1)	0.017(2)	-0.00024(1)	3.488(2)	0.0276(6)	-0.000120(4)
MM1	8.01(1)	0.098(5)	-0.00056(2)	4.54(2)	0.039(3)	-0.00037(2)	3.550(4)	0.0258(7)	-0.000124(5)

References

Larson, A. C., & Von Dreele, R. B. (2004). General structure analysis system (GSAS). *Los Alamos National Laboratory Report, Report*(LAUR), 86–748.

Levy, D., Diella, V., Dapiaggi, M., Sani, A., Gemmi, M., & Pavese, A. (2004). Equation of state, structural behaviour and phase diagram of synthetic MgFe2O4, as a function of pressure and temperature. *Physics and Chemistry of Minerals*, *31*(2), 122–129. https://doi.org/10.1007/s00269-004-0380-4

Plesa, A. C., Padovan, S., Tosi, N., Breuer, D., Grott, M., Wieczorek, M. A., et al. (2018). The Thermal State and Interior Structure of Mars. *Geophysical Research Letters*, *45*(22), 12,198-12,209. https://doi.org/10.1029/2018GL080728

Quinn, R.J., Valley, J.W., Page, F.Z., Fournelle, J.H. (2016). Accurate determination of ferric iron in garnets. *American Mineralogist*, 101 1704–1707. http://dx.doi.org/10.2138/am-2016-5695

Taylor, G. J. (2013). The bulk composition of Mars. *Chemie Der Erde*, *73*(4), 401–420. https://doi.org/10.1016/j.chemer.2013.09.006

Toby, B. H. (2001). EXPGUI, a graphical user interface for GSAS. *Journal of Applied Crystallography*, *34*(2), 210–213. https://doi.org/10.1107/S0021889801002242

Tsuchiya, T. (2003). First-principles prediction of the P - V - T equation of state of gold and the 660-km discontinuity in Earth's mantle . *Journal of Geophysical Research: Solid Earth*, *108*(B10), 311–328. https://doi.org/10.1029/2003jb002446